1328

University of Neuchâtel
Institute of Microtechnology

Integrated Optical Sensor Modules

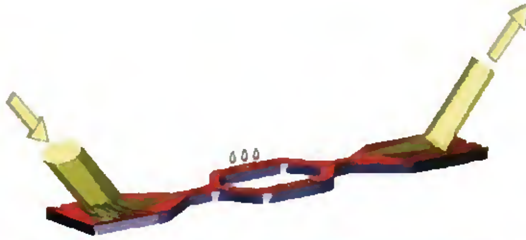

Dissertation

Submitted to the Faculty of Sciences of the University of Neuchâtel
to obtain the degree of Doctor of Sciences

by

Lothar U. Kempen
Dipl.-Ing. TH

July 1996

Université de Neuchâtel

Institut de Microtechnique

INTEGRATED OPTICAL SENSOR MODULES

MODULES DE CAPTEUR OPTIQUE INTÉGRÉ

Thèse

Présentée à la Faculté des Sciences pour obtenir le grade de Docteur ès Sciences

par

Lothar U. Kempen
Dipl.-Ing. TH

Neuchâtel, juillet 1996

IMPRIMATUR POUR LA THÈSE

Modules de capteur optique intégré.

de M. Lothar Kempen

UNIVERSITÉ DE NEUCHÂTEL

FACULTÉ DES SCIENCES

La Faculté des sciences de l'Université de Neuchâtel sur le rapport des membres du jury,

Messieurs N. de Rooij, H.-P. Herzig, R. Kunz (PSI-Zürich) et Mme U. Spichiger (ETH-Zürich)

autorise l'impression de la présente thèse.

Neuchâtel, le 22 juillet 1996

Le doyen:

R. Dändliker

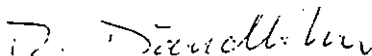

Preface

The following thesis was written during my employment as scientific assistant and PhD student at the optics group of the Paul Scherrer Institute (PSI) in Zurich.

I would like to thank Prof. Dr. N.F. de Rooij, director of the Institute for Microtechnology (IMT) at the University of Neuchâtel, for supervising my work and for helpful discussions. I gratefully acknowledge the beneficial hints of his collegues at the IMT, in particular Dr. Bart van der Schoot and Dr. Philippe Arquint.

Especially I want to thank Dr. Rino E. Kunz, who was my supervisor at the Paul Scherrer Institute Zurich, for introducing me to the field of integrated optical sensing and for imparting some of his scientific knowledge, instinct and enthusiasm to me.

I owe thanks to Dr. Karl Knop, director of the department for applied solid state physics of PSI, for giving me the opportunity to join the team at PSIZ. Many thanks go to M.T. Gale, head of the optics group, for many helpful discussions.

My collegues deserve acknowledgement for the friendly and "innovative" atmosphere in the laboratory and for their helpfulness in solving minor and major problems. To name a few of the many persons who supported my work, I would like to thank Bruno Graf, Bernd Maisenhölder, Otte Homan and Helmut Schütz for invaluable tips concerning process technology; Claus Heine and Thomas Hessler for many helpful discussions and Jörn Pedersen for many programming hints. The workshop crew, Max Derendinger, Ernst Meier and Urs Bruhin, was always helpful in finding solutions even for unusual mechanical demands. I would like to acknowledge Richard Stutz for performing the electroplating and for various useful tips, Daniel Jeggle for the e-beam evaporation of metal layers and Dr. Bernard Curtis and Roland Widmer for many hints about reactive ion etching.

The collaboration with the Swiss Center for Electronics and Microtechniques in Neuchâtel was very fruitful; I want to thank Dr. P. Sixt and J.-M. Mayor for their effort for obtaining excellent structures.

I would like to thank the team of the Centre for Chemical Sensors, Biosensors and (Bio-) analytical chemistry at the Swiss Federal Institute of Technology (ETH) in Zurich for the pleasant collaboration, especially Dr. Ursula Spichiger for accepting the Co-referate for my thesis and Michael Linhoff for his helpfulness and enthusiasm in night-lasting experimental series.

I want to acknowledge Dr. J. Edlinger of Balzers AG for performing optical coatings for us and for helpful informations.

Many thanks go to Hans Sigg and Klaus Thelen and the other collegues in the "PSI Running Team" for helping me clearing my head in our noontime-runs. I also enjoyed being part of the PSI band "PSIZzlers", and want to gratefully acknowledge the other members, Luca Baraldi, Rino Kunz, Jörn Pedersen, Markus Rossi, Peter Seitz and Jürgen Söchtig for the good time we had playing together.

Finally, I want to thank my wife Conny for supporting my work in many ways, thus also enabling the success of this thesis.

List of publications

In the range of this thesis, the following publications were made by the author :

R.E. Kunz and L.U. Kempen, "**Miniature Integrated Optical Sensors,**" Proc. SPIE, Vol. 2068, 69-86 (1994).

R.E. Kunz, J. Edlinger, B.J. Curtis, M.T. Gale, L.U. Kempen, H. Rudigier, and H. Schütz, "**Grating Couplers in Tapered Waveguides for Integrated Optical Sensing,**" Proc. SPIE, Vol. 2068, 313-325 (1994).

L.U. Kempen and R.E. Kunz, "**Miniature Integrated Optical Refractometer Chip,**" Proc. SPIE, Vol. 2208, 124-129 (1994).

L.U. Kempen, R.E. Kunz and M.T. Gale, "**Micromolded Structures for Integrated Optical Sensors,**" Proc. SPIE, Vol. 2639, 278-285 (1995).

L.U. Kempen and R.E. Kunz, "**Replicated Mach-Zehnder Interferometers with focusing grating couplers for sensing applications,**" submitted to Sensors and Actuators B (1996).

Contents

1. SUMMARY **1**

2. INTRODUCTION **3**

3. THEORETICAL FUNDAMENTALS AND DESIGN **5**

3.1. EVANESCENT WAVE SENSORS 5
3.1.1. The dielectric slab waveguide 5
3.1.2. Evanescent wave sensors 8
3.1.3. Chemically sensitive membranes 11
3.2. THE INTEGRATED OPTICAL LIGHT POINTER SENSOR 16
3.2.1. Linear grating couplers 16
3.2.2. Grating coupler sensors 17
3.2.3. Principle of the integrated optical light pointer 19
3.2.4. Chirped grating couplers 21
3.2.5. Dctection of the mode position 22
3.2.6. Grating design considerations 27
3.2.7. Light sources 28
3.2.8. Measurement cell design 29
3.2.9. Adaptation for micropumps 30
3.3. MACH-ZEHNDER INTERFEROMETER SENSORS 32
3.3.1. Principle of the Mach-Zehnder sensor 32
3.3.2. The stripe waveguide 33
3.3.3. Focusing grating couplers 36
3.3.4. Concept and design of the IO interferometer sensor 40
3.3.5. Passivation and sealing layers 43

4. FABRICATION OF THE COMPONENTS **45**

4.1. SUBSTRATE PATTERNING TECHNIQUES 45
4.2. GRATING COUPLER FABRICATION 46
4.2.1. Linear grating couplers 46
4.2.2. Chirped and focusing grating couplers 47
4.3. FABRICATION OF STRIPE WAVEGUIDES AND INTERFEROMETER STRUCTURES 49
4.3.1. Fabrication steps 49
4.3.2. Patterning of photoresist 49
4.3.3. RIE of Quartz 53
4.4. COMBINATION OF GRATING AND WAVEGUIDE STRUCTURE 56
4.5. REPLICATION 57
4.6. FILM DEPOSITION 61

4.7. DEPOSITION OF CHEMICALLY SENSITIVE MEMBRANES 62

5. COMPONENT CHARACTERIZATION AND MEASUREMENTS 64

5.1. CHARACTERIZATION OF THE COMPONENTS 64
5.1.1. Determination of planar and tapered waveguide parameters 64
5.1.2. Focusing grating coupler characterization 65
5.1.3. Characterization of stripe waveguides 67
5.2. REFRACTOMETRIC MEASUREMENTS 71
5.2.1. Sensor response on different Ethanol/Water mixtures 71
5.2.2. Measurements of chemical quantities 80

6. CONCLUSIONS AND OUTLOOK 84

7. REFERENCES 86

1. Summary

This thesis describes investigations on novel integrated optical sensor schemes based on specifically designed waveguide and grating coupler arrangements. The sensors are mainly aimed for determining the properties of liquid substances. The sensing principle is based on influencing the light guiding properties of an optical waveguide by substances brought into the evanescent field of the waveguide. Two different integrated optical arrangements are mainly investigated for converting this variation to an externally measurable quantity. The first approach is based on locally fulfilling the grating coupler resonance condition for coupling light into the waveguide, whereas the second one employs an integrated optical interferometer. The chip design is aimed on low cost, high sensitivity and the integration of measurement variables and a high degree of optical functions into the structure itself to reduce the requirements for external optical and mechanical elements.

The sensor chips were integrated into sensor modules together with external light sources and detectors. Results of measurements are shown that demonstrate the suitability of the sensor both as refractometer as well as chemical sensor. The demonstrated design of the structures together with their fabrication in polymer materials by replication techniques generally represent a step towards the low-cost fabrication of complex integrated optical components.

2. Introduction

The measurement of physical quantities by determining their effect on guided optical waves is of great interest for various applications. Some of the advantages of this approach are the high sensitivity and the immunity against electrical disturbances. Another aspect of increasing importance is the possibility of miniaturization of the sensor system. The waveguide exposed to the measurand can indeed be made very small, but often the measurement system consists of bulky external optical and mechanical components which are expensive and need careful adjustment for obtaining a measurement. By designing the optical structure properly, many of the functions and degrees of freedom provided by the external elements can be integrated into the optical sensor chip [1]. By this, the requirements for external optical and mechanical elements can be markedly reduced. A further advantage of miniaturizing the complete sensor structure is the possibility of placing several equal sensor systems very close to each other, enabling very precise referencing of the sensor signal with respect to unspecific parameter changes.

In many applications, like refractometry or chemical measurements in a liquid, the measurement contaminates the sensing structure, which has to be cleaned after each measurement. If the price of the integrated optical sensing structure can be held sufficiently low, it could act as a disposable part of the measurement system. It was already demonstrated in earlier works that stripe waveguide structures and optical diffraction gratings can be fabricated in polymer substrates by replication techniques, for instance hot embossing [2]. The use of waveguide structures for sensing applications, however, requires much higher differences in the refractive indices of the waveguide core and the substrate to achieve high sensitivity of the waveguide properties to ambient changes [3]. Unfortunately, this design also increases the effect of waveguide inhomogenities and surface roughnesses. It had to be investigated, if replication techniques still were applicable to produce highly sensitive stripe waveguide structures.

This work focuses on the investigation of novel integrated optical structures for sensing applications and their incorporation into a miniature measurement system. The design, fabrication techniques and characterization of the passive integrated optical devices are described as well as refractometric and chemical measurements in a sensor arrangement employing these structures.

3. Theoretical fundamentals and design

3.1. Evanescent wave sensors

3.1.1. The dielectric slab waveguide

A thin film deposited on a transparent dielectric substrate can act as an optical waveguide, if the refractive index of the film is higher than the

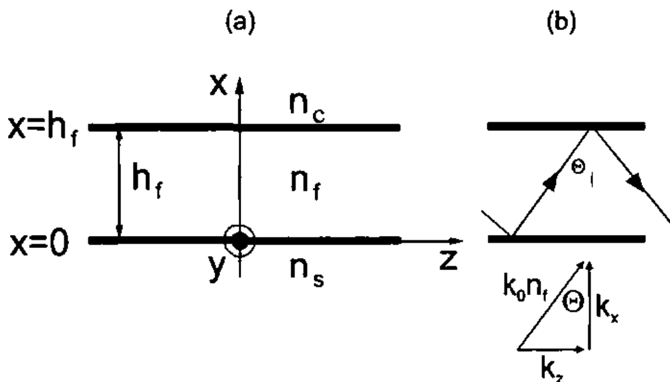

Fig. 1.(a) Basic configuration of an optical slab waveguide (b) Zig-zag wave propagating in the structure.

substrate and the cover index [4]. Fig. 1 shows the basic configuration of an optical slab waveguide with a thickness h_f of the guiding layer and infinite dimensions in the y- and z-direction. The refractive indices of the substrate, the waveguiding film and the cover medium are n_s, n_f and n_c, respectively.

The properties of the light propagating in the waveguide will now briefly be derived from the material properties and the dimensions of the structure, following the calculations in [5] and [6].

The light propagating in the waveguide can be described both by thc field equations obtained by solving the Maxwell equations and by a ray-optical

picture, rendering consistent solutions, as shown in [5]. The model of a 'zig-zag wave' in the waveguide was introduced in [7].

A ray of light propagating in the waveguide at an incident angle Θ onto the film surfaces is considered (cf. Fig. 1). The wave propagation constant in the wave-normal direction is $k_0 n_f$, with $k_0 = 2\pi/\lambda$, λ denoting the light wavelength in air. The propagation constants in the x and z directions are given by

$$k_x = k_0 n_f \cos\theta \tag{1}$$

$$k_z = k_0 n_f \sin\theta \tag{2}$$

The propagation constant $k_z = \beta$ is -for a lossless waveguide- the same as for a plane wave in an infinite medium with index $n_f \sin \Theta$. Therefore, an effective refractive index N is defined

$$N = n_f \sin\theta = \frac{\beta}{k_0}, \tag{3}$$

which actually is 'seen' by the guided mode propagating in z direction. To obtain a guided mode, i.e. total reflection at the film-substrate and film-cover interfaces, the effective index has to be smaller than n_f and larger than n_s and n_c, respectively.
The propagation constant k_x in x direction in the film is then given by

$$k_x = k_0 \cdot \sqrt{n_f^2 - N^2}. \tag{4}$$

Solving Maxwell's equations in a lossless, isotropic waveguide for a plane wave propagating in z direction yields two independent solutions for the components of the electric and magnetic field. The solution for the field components E_y, H_x and H_z is called TE (transverse electric field) mode, because the electric field has components perpendicular to the propagation direction only. Similarly, the solution for the H_y, E_x and E_z components is called TM (transverse magnetic field) mode.

The field distribution of the transverse electrical field of a TE mode (which is analogous to the magnetic field distribution of a TM mode) is given by [6]

$$E_y = E_c \cdot e^{-\gamma_c (x-h_f)} \quad \text{for the cover region } (x > h_f) \tag{5}$$

$$E_y = E_f \cdot \cos(k_x \cdot x + \phi_c) \quad \text{for the film region } (0 < x < h_f) \tag{6}$$

$$E_y = E_s \cdot e^{\gamma_s \cdot x} \quad \text{for the substrate region } (x < 0) \tag{7}$$

The distribution of the transverse electric field is sinusoidal in the film and exponentially decreasing in the cover and substrate layers. The propagation constants in x direction in the cover and substrate yield the field penetration depths :

$$\gamma_c = k_0 \cdot \sqrt{N^2 - n_c{}^2} \tag{8}$$

$$\gamma_s = k_0 \cdot \sqrt{N^2 - n_s{}^2} \tag{9}$$

and ϕ_c is given by

$$\phi_c = \arctan(\gamma_c / k_x). \tag{10}$$

The dispersion relation for this waveguide can be written in a compact form :

$$2 h_f k_x + \delta_{fs} + \delta_{fc} = 2\pi \cdot m, \tag{11}$$

which states that the total phase change for one round trip in the transverse waveguide direction has to be an integer multiple of 2π, m denoting the order of the mode. The total phase shift is determined by the propagation in the film ($2\ h_f\ k_x$) and the phase shifts due to the total internal reflection at the film/substrate (δ_{fs}) and at the film/cover (δ_{fc})interface.

The phase shifts at the interfaces are given by

$$\delta_{fs} = -2 \cdot \arctan\left[(\frac{n_f}{n_s})^{2\rho} \cdot \sqrt{\frac{N^2 - n_s^2}{n_f^2 - N^2}} \right] \tag{12}$$

$$\delta_{fc} = -2 \cdot \arctan\left[(\frac{n_f}{n_c})^{2\rho} \cdot \sqrt{\frac{N^2 - n_c^2}{n_f^2 - N^2}} \right] \tag{13}$$

where ρ determines the polarisation of the mode : $\rho = 0$ for TE mode and $\rho = 1$ for TM mode. Introducing equations (12) and (13) into (11) gives a formula that can be solved numerically to calculate the effective index from the waveguide parameters and vice versa.

3.1.2. Evanescent wave sensors

Since the light guided in the slab waveguide is not completely confined to the high-index core layer as described in the previous chapter, changes in the optical properties of the cover medium influence the light velocity in the structure. As it was demonstrated in [8], this effect can be utilized to intentionally influence the waveguide properties by the application of an external medium. It was shown in later works [9] that this principle also is suited to construct refractometric sensors, where the test substance is used as the cover medium of the waveguide, thus influencing the effective index of the waveguide structure (sec Fig. 2).

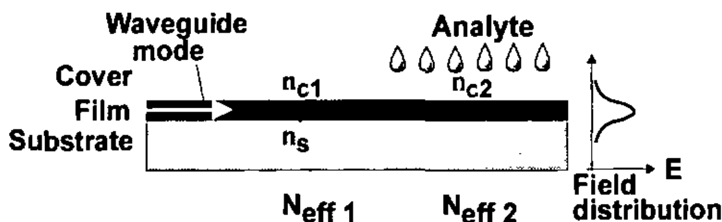

Fig. 2. Principle of the evanescent field sensor.

The conversion of a change in the refractive index of the cover medium n_c to a change in the effective refractive index N described by the derivative $\partial N/\partial n_c$ was evaluated for TiO_2/SiO_2-waveguides on glass substrates in [10]. Calculations based on the formulas given in Chapter 3.1.1 show that thin high-index films on low-index substrates lead to the highest sensitivities. In [11] hard, stable dielectric films with an index larger than 2 were investigated, showing high sensitivity and low drift effects. Fig. 3 (a) shows the calculated sensitivities for TiO_2 films on polycarbonate substrates for aqueous cover media and the wavelengths of $\lambda = 633$ nm and $\lambda = 785$ nm. The maximum values for $\partial N/\partial n_c$ in the range of 0.24 are achieved for film thicknesses of about 110 nm and 140 nm, respectively. Although these highest sensitivities are -of course- desirable for sensor applications, they also lead to increased losses at waveguide imperfections. Especially in stripe waveguides, where the mode is also laterally guided, this leads to high technological demands for low roughness of the sidewalls to achieve reasonable waveguide losses. For this reason, the application of films with some lower index might be necessary for stripe waveguides. In Fig. 3 (b), the sensitivity of TiO_2 / SiO_2 mixed oxide films ($n_c \equiv 1.8$) is shown. The maximum sensitivity of this waveguide type is still very high, about half the value of what can be achieved employing TiO_2 films.

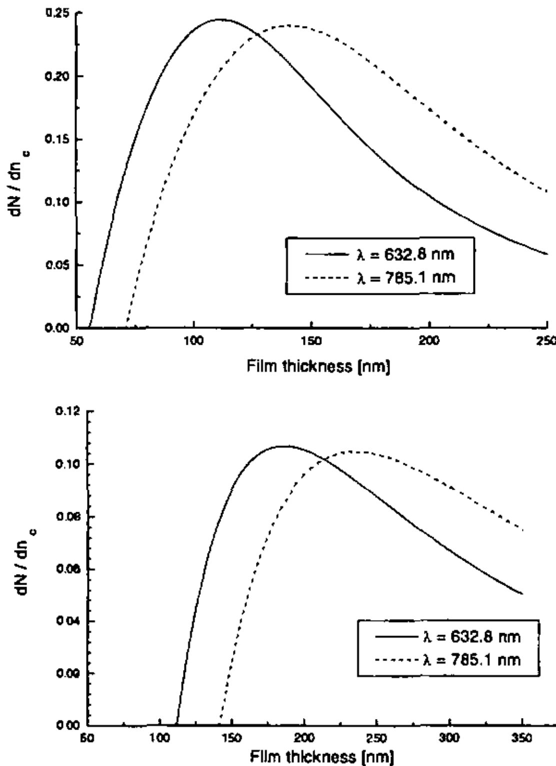

Fig. 3. Sensitivities of planar waveguides on polycarbonate substrates with water as cover medium; TM_0 mode.
Top : TiO_2 film, bottom : TiO_2/SiO_2 film.

Various optical arrangements exist to convert this change in the effective waveguide index N to an externally measurable quantity. In this work, two types of sensors were investigated. The first one is based on determining the resonance condition of a grating coupler by measuring the position of a locally excited mode (cf. Chapter 3.2), whereas the second type uses an interferometric setup (cf. Chapter 3.3).

3.1.3. Chemically sensitive membranes

The application of a cover layer to the waveguide which changes its optical refractive index upon the influence of a specific chemical substance, allows

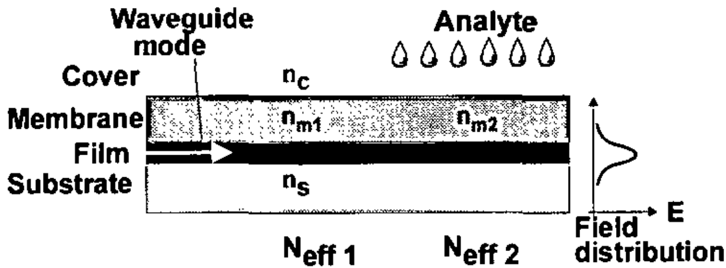

Fig. 4. Arrangement of an evanescent field sensor employing a chemically sensitive membrane.

the measurement of distinct chemical quantities (see Fig. 4). By choosing the thickness of the membrane significantly larger than the penetration depth of the evanescent field into the membrane, the sensing region is protected against possible disturbances caused by variations of the optical properties of the test substances. This is necessary to determine solely the impact of the chemical quantity of the analyte to be measured on the refractive index of the membrane, even when strongly absorbing or highly scattering substances are examined.

In the scope of this work, membranes sensitive for calcium ions (Ca^{2+}) were employed for the measurements. They were developed and supplied by the Centre for Chemical Sensors, Biosensors and (bio-)Analytical Chemistry of the Department of Pharmacy, Swiss Federal Institute of Technology (ETH), Zurich. Their function is described in detail in [12]. Therefore, only their basic working principle will be described here.

The membranes are based on embedding chemically sensitive substances into a plasticized polyvinylchloride (PVC) matrix, which thermodynamically acts like a liquid phase, providing a well defined distribution of all chemical species involved in the analyte recognition - process between the test solution and the membrane. The employed plasticizer in this case was

bis(2-ethylhexyl)sebacate (DOS). The substances being dissolved within this PVC matrix to achieve selective sensitivity towards a distinct analyte have to be highly lipophilic to avoid their migration into the test liquid.

Three substances are built into the plasticized PVC matrix :

- An 'ionophore' (L), a ligand which is highly selective for complexing a specific ion, in the employed system Ca^{2+} (ETH 1001).
- A 'chromoionophore' (C), an ionophore which changes its absorption spectrum significantly upon complexation of a specific ionic species. The substance used in the system (ETH 5294) changes its spectrum within the visible area highly selectively to Hydrogen ions (H^+), which implies high basicity.
- Lipophilic 'anionic sites' (R^-), negatively charged ions, which maintain electroneutrality of the membrane during the ion-exchange process with the liquid.

The basic principle of the optode membrane is to combine the high selectivity of the ionophore ETH 1001 for Ca -Ions with the high absorbance shift upon protonation of the chromoionophore ETH 5294 by utilizing a Ca^{2+} / H^+ - ion exchange process between the membrane and the aqueous analyte solution. By this, the need for a single chromoionophore with high selectivity to Ca -Ions and a large absorbance shift is circumvented.

When the membrane is in contact with an aqueous solution containing Ca^{2+}, an ion-exchange reaction between the membrane (org) and the solution (aq) takes place, as described by the following equation:

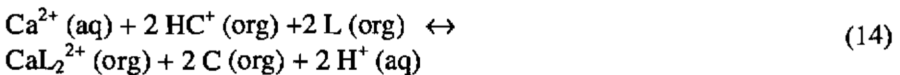

$$Ca^{2+}\,(aq) + 2\,HC^+\,(org) + 2\,L\,(org) \leftrightarrow CaL_2^{2+}\,(org) + 2\,C\,(org) + 2\,H^+\,(aq) \tag{14}$$

The equilibrium constant K_{exch} of this reaction is given by

$$K_{exch} = \frac{(a_{Ca^{2+}})\,[HC^+]^2\,[L]^2}{[CaL_2^{2+}][C]^2\,(a_{H^+})^2} \tag{15}$$

with activities being regarded for the species within the aqueous solution and concentrations for those substances in the membrane. This is based on the assumption of constant activity coefficients of all species in the organic phase.

The electroneutrality of the membrane is provided by the anionic sites R^- with the total concentration

$$[R^-] = [HC^+] + 2[CaL_2^{2+}] \tag{16}$$

The absorbance A of the membrane is determined by the degree of deprotonation α, the concentration ratio of unprotonated to total chromoionophore present :

$$\alpha = [C]/C_T \; ; \qquad 1-\alpha = [HC^+]/C_T \,, \tag{17}$$

with C_T denoting the total concentration of the chromoionophore in the membrane.
A is given by

$$A = A_1 \alpha + A_0 (1-\alpha) \tag{18}$$

where A_1 and A_0 are the absorbance values for $\alpha = 1$ and $\alpha = 0$, respectively. By adding the mass balance equations

$$C_T = [C] + [CH^+] \qquad \text{and} \tag{19}$$

$$L_T = [L] + [CaL_2^{2+}] \,, \tag{20}$$

the activity of the Ca - Ions can be calculated from α by combining equations (15-20) to the formula

$$a_{Ca^{2+}} = \left(a_{H^+}\right)^2 \cdot K_{exch} \cdot \left(\frac{\alpha}{1-\alpha}\right)^2 \cdot \frac{R_T - (1-\alpha)C_T}{2 \cdot (L_T - \{R_T - (1-\alpha)C_T\})^2} \tag{21}$$

It is obvious by this equation, that the optical determination of the Ca^{2+} activity in a sample solution only is possible if the exchange equilibrium of H^+ - ions between the membrane and the analyte solution remains constant or is exactly known, i.e. the pH value is buffered or is measured simultaneously.

Furthermore, if the precise measurement of Ca^{2+} - concentrations is desired, as in most practical cases, the activity coefficients of the Ca^{2+} - as well as the H^+ - ions within the analyte solution have to be held constant, which can be achieved approximately by a constant ionic background (i.e. a well-defined ionic strength), as provided by buffering.

Measurements of the spectral absorbance of the membranes in dependency of the concentration of Ca -Ions were presented in [13]. By performing the Kramers-Kronig transformation on the measured absorbance spectra, the dispersion curves of the membranes as a function of the Ca^{2+} concentration were obtained in this paper. Both diagrams are depicted in Fig. 5. The maximum shift of the refractive index upon concentration variations was predicted from the calculated curve for a wavelength of about 690 nm, which refers to the deprotonated form of the chromoionophore. Measurements performed at this wavelength yielded a shift of the membrane refractive index of $\Delta n_m \approx 4*10^{-3}$ upon changing the Ca^{2+}- concentration in the test solution from 10^{-5} mol/l to 10^{-1} mol/l [13]. It also can be seen from the curve that the absorbance is quite high for this wavelength. Since the transformation in the Hilbert space described by the Kramers-Kronig equation relies on the spectral range of the input data, which ideally is infinite, but in this case is identical with the spectral interval of the calculated values for the refractive index, the calculated dispersion curve has to be interpreted only as a qualitative description.

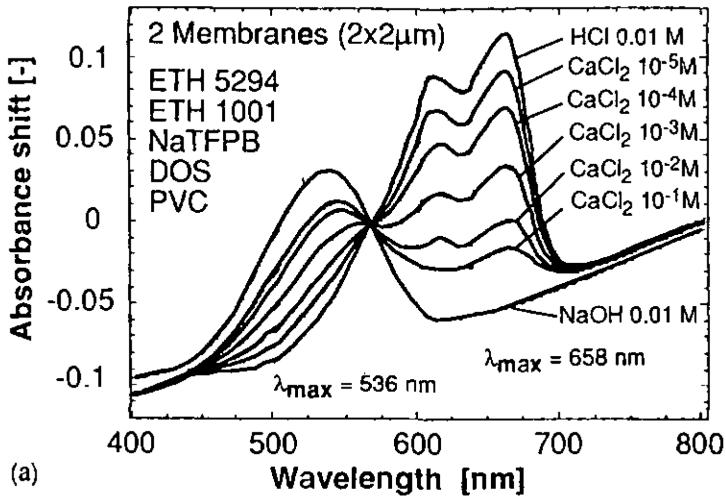

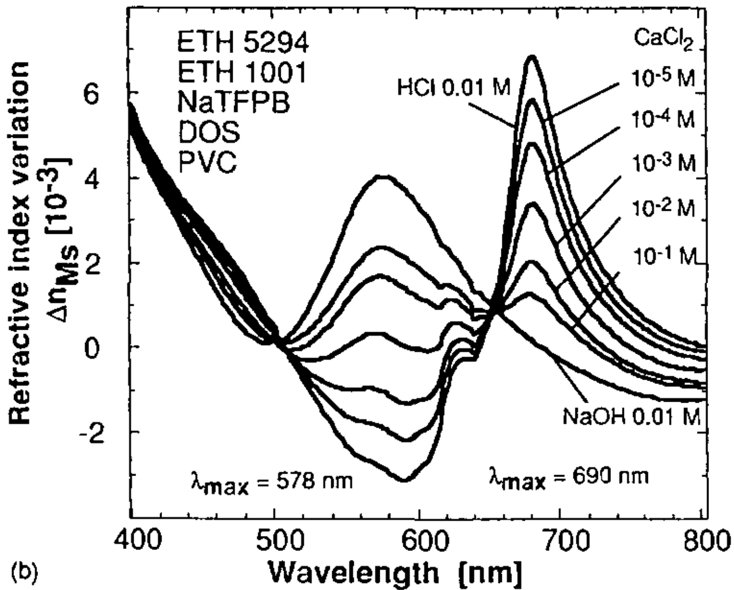

Fig. 5. (a) Measured absorption of the optode membrane, (b) calculated dispersion curve upon changes of the Ca^{2+} - concentration [13].

3.2. The integrated optical light pointer sensor

3.2.1. Linear grating couplers

The coupling of light in free space to a guided wave in a slab waveguide by means of a diffraction grating was first reported in [14]. A grating coupler in a planar waveguide structure basically is the special case of a diffraction grating with an output angle of 90° and an output medium of index N with N being the effective index of the waveguide.

The condition for resonant coupling of a free-space beam in a medium of index n_a into the waveguide of effective refractive index N_g (see Fig. 6) is given by

$$\Lambda \cdot (N_g - n_a \cdot \sin \Theta_i) = m_g \cdot \lambda \tag{22}$$

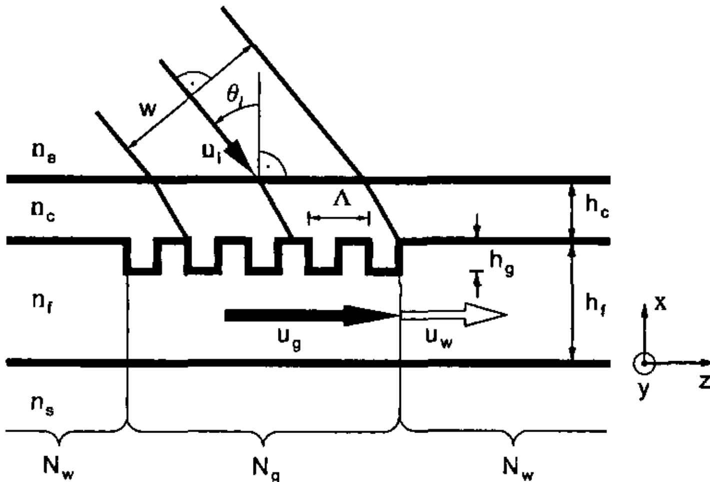

Fig. 6. Basic configuration of a grating coupler in a slab waveguide.

with Λ being the grating period, θ_i the input angle, m_g the grating diffraction order and n_a the refractive index of the ambient medium. For a precise determination of the resonance condition for coupling to the waveguide, it has to be taken into account that a grating of finite depth h_g influences the waveguide parameters, leading to slightly different effective refractive indices N_w in the undisturbed waveguide and N_g in the grating region. Whereas the effective index of the undisturbed waveguide can be calculated by the formulas given in chapter 3.1.1, the determination of the effective index in the grating region requires calculations based on rigorous diffraction theory [15,16,17] to obtain precise results. To avoid the time-consuming rigorous calculation, an approximate solution can be found by assuming the grating region as a 4-layer waveguide, the grating being replaced by an 'equivalent layer' of thickness h_g and an intermediate refractive index with a value between the values of the adjacent media. A comparison of the results from this approximation for different formulas to obtain the index of the intermediate layer and rigorous calculations was recently presented in [18].

3.2.2. Grating coupler sensors

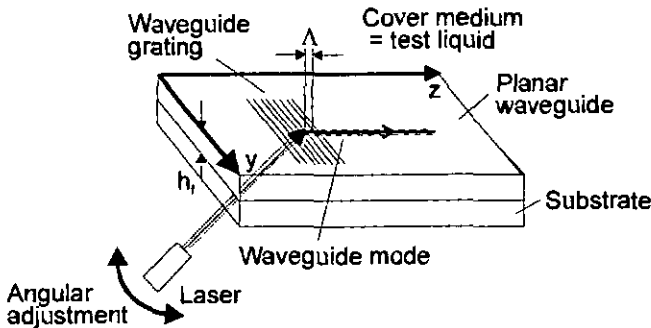

Fig. 7. Principle of the input grating coupler sensor.

The dependency of the grating coupling condition on the effective refractive index N can be employed for measuring a change of N. In many cases, the coupling angle is used as the adjustable parameter, from which the effective

index N can be calculated, if the waveguide and grating parameters are known. In Fig. 7, an input grating coupler is employed, leading to a measurement by adjusting the angle of the input beam to the resonance condition, as demonstrated in [19]. This setup has the disadvantage of needing a precise goniometer table that has to be adjusted to achieve a measurement. Employing an output grating coupler for the measurement avoids this necessity [20], when a position sensor is placed in some distance of the chip, determining the beam position as a measure for the output angle. This arrangement still does not have the possibility to be built very compact, since a considerable distance between the optical waveguide and the position is necessary to convert the angular shift into a measurable position shift.

When employing a waveguide grating coupler as an evanescent field sensing device, the disturbance of the waveguide by the grating has to be included in the calculation of the resonance condition, as described in the previous chapter. When employing the thin grating approximation, assuming an undisturbed waveguide, the characterization of the chip by measuring the resonance condition yields a slightly deviated value for the physical refractive indices and dimensions of the waveguide structure. When the waveguide is employed as a sensor, these values are then employed to re-calculate changes in the cover refractive index by determining the resonance condition. The error introduced into the model by this assumption can be held low by characterizing the waveguide structure with a cover medium of an index very close to the one applied in the sensor measurements. This method was employed for the refractometric measurements presented in chapter 5.2.

In the grating coupler sensor, the section of the waveguide used for the measurement is confined to the grating region. Due to this fact, increasing the sensitivity by enlarging the interaction length between the medium and the waveguide is only possible by increasing the grating length. This can be done only to a certain limit, where the light coupled to the waveguide in the rear part of the grating starts to be coupled out by the remaining part of the grating, thus reducing the efficiency of the grating coupler. The method of producing very large, very weakly coupling gratings is only applicable to a certain extent due to practical considerations.

3.2.3. Principle of the integrated optical light pointer

Equation (22) describes the resonance condition for coupling into the waveguide in every point of the grating coupler. If one of the parameters varies along the grating lines with all other parameters held constant, the resonance condition is only fulfilled at a certain position on the chip (see Fig. 8). At this place, a locally excited waveguide mode, the "integrated optical light pointer" beam is excited, changing its position y_b with the change of any of the parameters N, Λ, λ and θ_i in formula (22). The concept of using the lateral position of the excited mode as an on-chip measuring variable was first proposed in [1].

Onc possibility to build a sensor based on this principle is to implement a spatial variation of the effective index N into the waveguide. This can be achieved for instance by a varying thickness and/or refractive index of the waveguiding film. The light pointer position then can be used as a sensor for the effective index, grating period, light wavelength and input angle.

In this work, the application of the light pointer sensor principle for the detection of changes in the effective index N was investigated. As described in chapter 3.1.2, a change in the index of the cover medium of the waveguide leads to a change in thc effective index. If the input grating G_i is illuminated

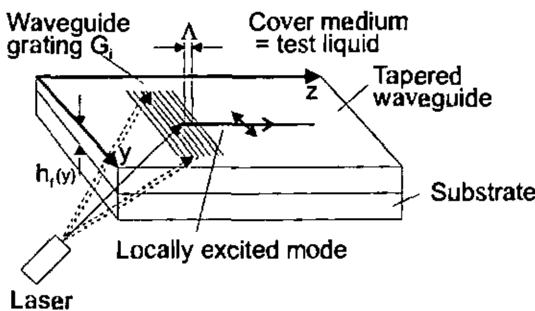

Fig. 8. Principle of the integrated optical light pointer.

by an expanded laser beam at a fixed angle θ_i, the position of the light pointer is a measure for the refractive index n_c of the cover medium (see Fig. 8). The mode can be coupled out by means of a second grating, the mode position being determined by a position detector, like a line CCD or a PSD (Position Sensitive Device), without the need of any additional optics and without the inherent neėd for a distance between the output grating and the detector, as described in Chapter 3.2.2.

The travel of the light pointer upon changes of the cover index is dependent on the slope of the thickness of the waveguiding film. A flat slope forces the light pointer to a perform a large lateral shift to move to the new position where the resonance condition is fulfilled. The width of the lightpointer also depends -among other parameters - on the slope of the waveguide : a flat slope is related to a wide light pointer, whereas a steep slope generates a narrow beam. Obviously, the general tradeoff between measurement range and resolution also has to be done, because every gain in resolution decreases the measurement range. Thc sensitivity of the chip could be even be tuned by varying the slope locally to be very accurate in a small region but to cover a large range with low resolution outside that region. The light pointer width defines the limits of those variations due to practical reasons : A light pointer width coming close to the lateral dimensions of the chip makes the precise detection of lateral displacements almost impossible; a light pointer width close to zero makes the beam almost undetectable and the position determination might be disturbed even by slight inhomogenities in the waveguide, if the narrow mode is currently at this position.

3.2.4. Chirped grating couplers

In a chirped grating coupler, the grating period Λ varies along the grating lines[1]. This leads to another possibility to implement a spatial variation of the resonance parameters for coupling to a planar waveguide, leading to the

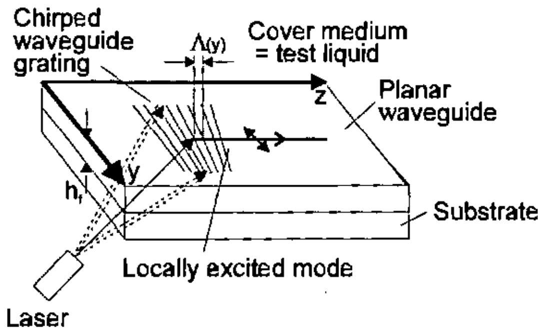

Fig. 9. Light pointer excitation by a chirped grating coupler.

excitation of an integrated optical light pointer [1] (see Fig. 9). The spatial variation of the grating period instead of the effective index as described in the last chapter has the advantage of constant sensitivity dN/dn_c in every point of the waveguide as well as the high reproducibility of the waveguide pattern, when replication techniques are employed for fabrication. The fabrication of the grating pattern is challenging, since for a highly sensitive sensor, the variation of the grating period has to be very small to lead to a large travel of the light pointer to match the grating resonance condition. The production method for the chirped grating structures is described in chapter 4.2.2.

[1] The term 'chirp' stems from the variation in spatial frequency, analogous to the frequency variation of a tone.

3.2.5. Detection of the mode position

3.2.5.1. Position sensor considerations

In first experiments the lateral position of the IO light pointer was determined by imaging the scattered light of the mode with an objective on a CCD camera. If the mode is coupled out by a second grating, the spatial resolution and the intensity of the emerging light pattern can be enhanced. In the realized setup, the determination of the lateral position of the outcoupled light was achieved by employing either a linear CCD array or a position-sensitive detector (PSD). The advantages of the linear CCD array are the very high sensitivity to low light levels, the fixed and well-determined size and position of the detector elements and the acquisition of the whole irradiation pattern, enabling the separation of different intensity maxima. The disadvantages are the complicated clock generation and the necessity of evaluating the acquired irradiation pattern to get the position of the mode.

The main advantage of the PSD is the direct conversion of light into electrical signals corresponding to the position of a light spot. By performing the division of the difference and the sum of the two PSD signals, a voltage corresponding to the "center of gravity" of the measured light distribution is obtained without the need for additional signal processing. This leads to a quick determination of the mode position. The drawbacks of employing a PSD detector are the nonlinearity of the PSD itself and of the subsequent electronics, leading to the necessity for calibration of the whole system and to a slight dependence of the position signal of the total light intensity. Another drawback is the impossibility of dealing with more than one intensity maximum, leading to incorrect results in position determination in the presence of stray light.

3.2.5.2. CCD detector setup

Taking into account the advantages of the linear CCD array considered in 3.2.5.1, this device was employed for most mode position measurements. The CCD chip was a Toshiba TCD 131D, a 2048-element linear image sensor[2] with a pixel size of 14 µm by 200 µm and 14 µm pixel pitch. The rectangular profile of the pixels increases the light sensitive area by a factor of 14 in one dimension while maintaining the spatial resolution of 14 µm in the other dimension. Since no commercial evaluation board was available for this chip, the clock generation and signal processing electronics had to be built in the laboratory.

The CCD signal was pre-amplified directly at the detector chip, electronically symmetrized in a circuit close to the detector and connected by a 2 m long cable to a PC equipped with an analog/digital converter (ADC). The data acquisition board was a Keithley DAS1600 with 12 bit resolution and a sample rate of up to 100 KSamples per second. In the first setup, this maximum pixel clock rate limited the frame rate to 100 KHZ/2094 = 48 Hz, leading to a sensor integration time longer than 21 ms. Due to this fact, the light sensitivity of the chip was too high and the signal to be detected had to be attenuated by filters to avoid clipping.

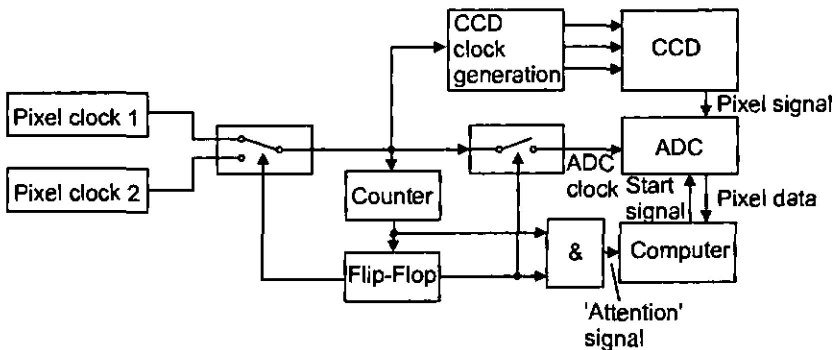

Fig. 10. Block diagram of measurement system using CCD clock switching.

[2] In this chip 2048 of the total 2094 pixels are exposed to light; the remaining pixels are used for referencing.

In a second design for the clock generation unit, this problem was avoided by using two cycles with different clock rates for the CCD readout (see Fig. 10). In the first cycle, the CCD pixel clock is set to 1..2 MHz (Pixel Clock 1), thus leading to integration times in the millisecond range. During this phase, the clock is not transmitted to the ADC. The second phase begins when the counter has counted to the total number of pixels. In this phase, Pixel Clock 2, having a reduced frequency of about 70 kHz, is transmitted to the CCD and is also used as external ADC clock, enabling the slow readout of the image generated in the shorter first exposure period. By this method, the sensitivity of the CCD detector can be set by choosing the clock rate during the first exposure period without the constraints given by the maximum A/D conversion rate. An 'attention' signal is generated every time the system switches to the fast clock rate. The computer then can activate the ADC at any time during this phase, while the conversion itself starts synchronized when the clock signal is turned on. The reduction of the effective frame readout rate by sampling only every second image is negligible, since the overall measurement speed is mostly constrained by the time required for the computer evaluation of the sampled data.
In the computer controlling the measurement setup, a Gaussian curve with a superimposed linear slope represented by the formula

$$I(y) = A + By + C\exp\left[-D(y - y_b)^2\right] \tag{23}$$

was automatically fitted to the data representing the CCD irradiation pattern every time a new frame was sampled, the whole measurement and calculation procedure requiring about two seconds. The linear term with coefficients A and B is used to model the background irradiance; the height, width and position of the peak being modelled solely by the parameters C, D and y_b , respectively. The algorithm for the fit procedure was taken from [21].

By using the position of the maximum of the Gaussian curve y_b as the measure for the lateral position of the light pointer, a spatial resolution in the micrometer range, significantly better than the CCD pixel pitch of 14 µm, was achieved. The calculated parameters of the fit function were listed and saved in a table together with the time of the data acquisition. This system enabled long-time measurements of the light pointer position.

3.2.5.3. PSD detector setup

A one-dimensional position sensitive device is basically a long PIN-photodiode[3], incorporating one common contact at the n-layer and two contacts at both ends of the p-layer. When this structure is illuminated by a light spot at a certain position on the photosensitive surface, the photocurrents measured at the two contacts of the p-layer are a measure for the position of the light spot along the axis of the PSD [22]. In two transimpedance amplifiers, the two photocurrents are converted to the voltages V1 and V2. To get an intensity-independent position signal, the position information derived from the difference of the two signals has to be normalized by the total intensity, i.e. the sum of the two voltages. This process was performed by a commercial electronic circuit[4], so that the position signal directly was available for further processing.

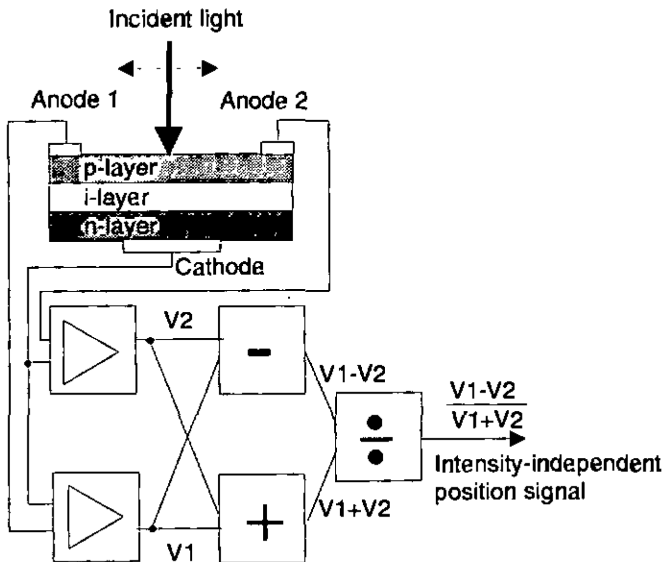

Fig. 11. Schematic diagram of a PSD with evaluation circuit for generating a position signal.

---

[3] The capital letters denote the doping of the silicon layers : p-doped / intrinsic / n-doped.

[4] Hamamatsu Signal Processing Circuit C3683-01

3.2.5.4. Detector arrangement

In the first experiments, the light coupled out from the sensor chip was reflected by a mirror and directed onto the detector chip with or without an imaging lens (see Fig. 12). The use of a mirror enabled to choose a small

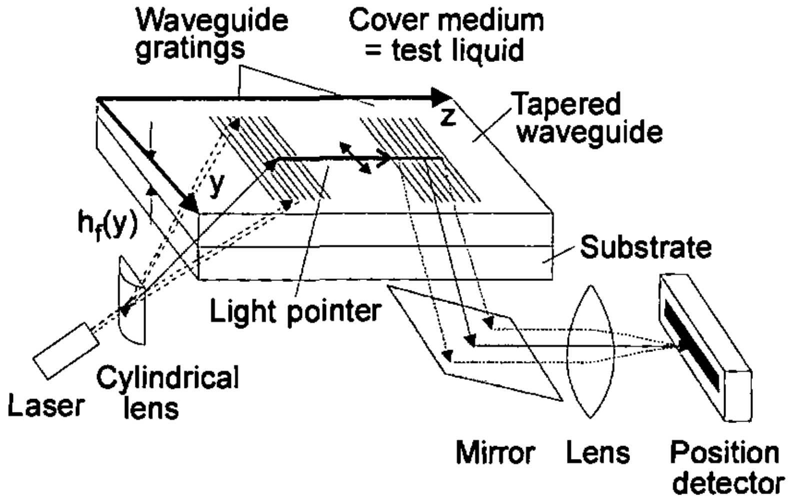

Fig. 12. Experimental setup for the light pointer sensor.

angular region near the collimated output beam to reduce the influence of scattered light and other reflections on the measured irradiance pattern. It also allowed to measure the mode position when the angles of input and output beam were very close to each other, thus avoiding the blocking of the input beam by the detector. To realize a compact assembly of the sensor device, in a second design the position detector was mounted on a revolving arm that was fixed to the measurement cell at the lateral position of the output coupler (see Fig. 13). The "sensor head" was adjustable in three dimensions and could be fixed after adjustment. This arrangement allowed the placement of the position detector very close to the integrated optical chip.

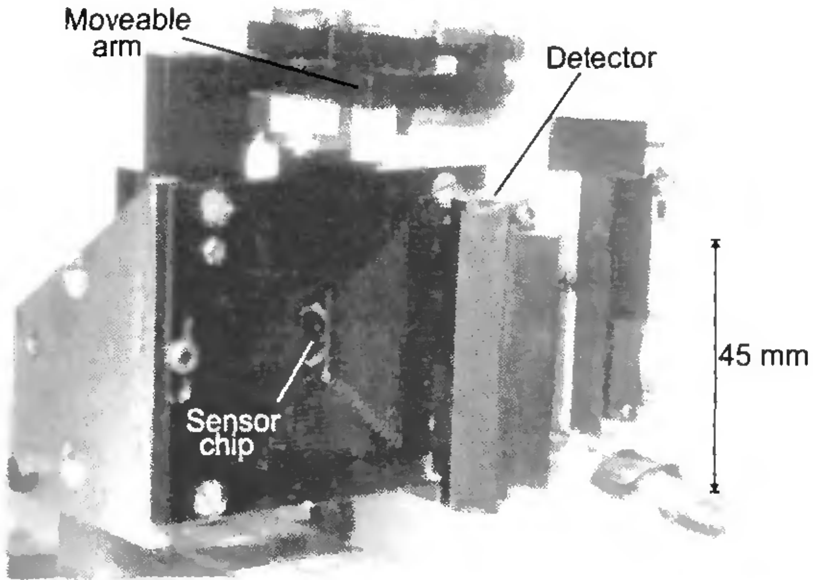

Fig. 13. Photograph of the detector arrangement for the compact sensor cell.

3.2.6. Grating design considerations

In the sensor chips used in this work, the input and output gratings had different grating periods to avoid disturbance of the mode detection by the light reflected from the input beam. Usually, at least one of the gratings on the sample could be used to couple into the waveguide by employing the second diffraction order ($m_g = 2$ in Eq. 22). This could be utilized in the case of highly absorbing layers placed on the waveguide, as in the case of the chemically sensitive membranes (cf. Chapter 3.1.3). The high absorption attenuated the mode too much to be coupled out by the second grating. When the first diffraction order of the same grating is used for input and the second order for output or vice versa, the light pointer excited in the grating region propagates only a very short distance until it is coupled out. A disadvantage of this method is that the higher diffraction order generated by the grating itself superposes the waveguide mode coupled out in the same direction, reducing the signal-to-noise ratio of the detector.

3.2.7. Light sources

The wavelength of the illuminating light source must be known precisely for calculating the cover refractive index as a function of the lateral position of the light pointer. A finite bandwidth of the source leads to an increased width of the light pointer.

For the evaluation of the sensor system, three different light sources were employed. A red HeNe-laser with a wavelength of $\lambda = 632.8$ nm was used as a reference due to its high wavelength stability (thermal drift ~ 2.5 pm/°C) and small bandwidth (typically ~2 pm for a multimode laser) [23]. The output power was about 10 mW.

To build a miniaturized system, a semiconductor laser diode as light source is best suited due to its size and weight. A laser diode with a wavelength $\lambda = 785.1$ nm was used in the system. Laser diodes at this wavelength are very low-cost devices due to their application in CD players. To obtain good wavelength stability, the device was temperature-controlled employing a Peltier element. The operating temperature was chosen by monitoring the light of the laser diode by means of a spectrometer while sweeping the device temperature in an interval of some centigrades. At certain temperatures "mode-hops", fast transitions between different longitudinal modes in the laser cavity occurred. The operating temperature of the laser was then chosen in between those temperatures to guarantee good wavelength stability. With a temperature stabilization to about 0.1 °C and a temperature coefficient of the laser diode wavelength of ~ 60 pm/°C, a wavelength stability of about 6 pm was achieved.

3.2.8. Measurement cell design

In the measurement cell, the liquids to be measured are brought into contact with the waveguide structure. The basic configuration of the cell is shown in Fig. 14. The front of the cell is formed by the optical chip with the waveguiding film inside to allow contact of the film with the test substance, hence the light enters and exits through the substrate. The cell temperature has to be monitored continuously, since the temperature coefficient of the refractive index is quite high for liquids, as an example, ethanol changes its refractive index by about $-4x10^{-4}$ K^{-1}. For this purpose a temperature sensor was built into the cell, in this case a 'Pt100' element, which consists of a platinum resistor with a resistance of 100 Ω at 0 degrees Celsius.

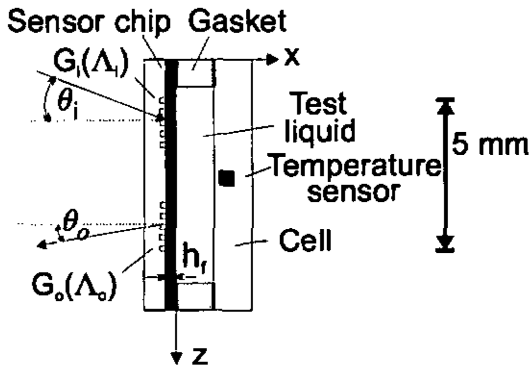

Fig. 14. Basic configuration of the measurement cell.

In principle, the cell volume should be as low as possible to minimize the required amount of test substance; in practise, each of the cell dimensions has to obey certain constraints. In the sensor based on the light pointer principle, the input and output grating should both be covered with the measured liquid. The grating length exposed to the test substance defines the range of the possible light pointer excursion, hence the measurement range. The height of the channel for the liquid flow is absolutely limited by the penetration depth of the guided light into the liquid, but in the realized device it was chosen larger (200 μm) to avoid problems with the liquid flow

in extremely thin channels. The gratings on the test chip were 2 mm wide, being separated by 1 mm. A light pointer excursion of 15 mm was found to be sufficient for the test measurements. These dimensions gave a cell volume of 15 microliters and a cross-sectional area of 1 mm^2. The flow channel was tapered at the liquid input and output to form a "funnel" to obtain a smooth transition from the circular teflon tube connected to the measurement cell into the rectangular flow channel. The avoidance of abrupt changes in the cross-section of the liquid flow prevented outgasing of the test liquid due to pressure changes.

The cell was completely fabricated of black delrin (polyacetal), which has good mechanical stability and is inert to ethanol, which was used as test solution. This was checked by measuring the refractive index of ethanol before and after placing delrin chips into it for some days.

3.2.9. Adaptation for micropumps

The incorporation of a pump for liquid transportation into the sensor enables the stand-alone operation of the system. Miniature pumps with a size of 22 x 22 x 2 mm were developed and supplied by the Institute of Microtechnology, Neuchâtel, Switzerland. A measurement cell was built incorporating such a device in the liquid stream, having the same size as the previously designed cell.

The function principle of the micropump is depicted in Fig. 15 [24]. The pump consists of a glass plate of 1.5 mm thickness, which acts as the base plate of the system, and a thinner glass plate of 0.3 mm thickness, which serves as the pump membrane. Between the plates a micromachined silicon chip is installed, which is shaped to act as input and output valve. A piezo disk is glued onto the thin glass membrane by using conductive epoxy. When the piezo is driven by a square wave voltage of about 200 V, the liquid is pumped from the left to the right chamber and out of the outlet hole upon bending of the glass membrane by the piezo disk. When the strain is relaxed, the left chamber is filled with new liquid from the inlet hole. With an actuation frequency of 400 Hz, the devices perform liquid pumping with a flow rate of up to 1 ml per minute. In the normal operation mode, the flow

speed is set to about 200 µl /min, so that the contents of the measurement cell described in 3.2.8 can be exchanged in about four seconds.

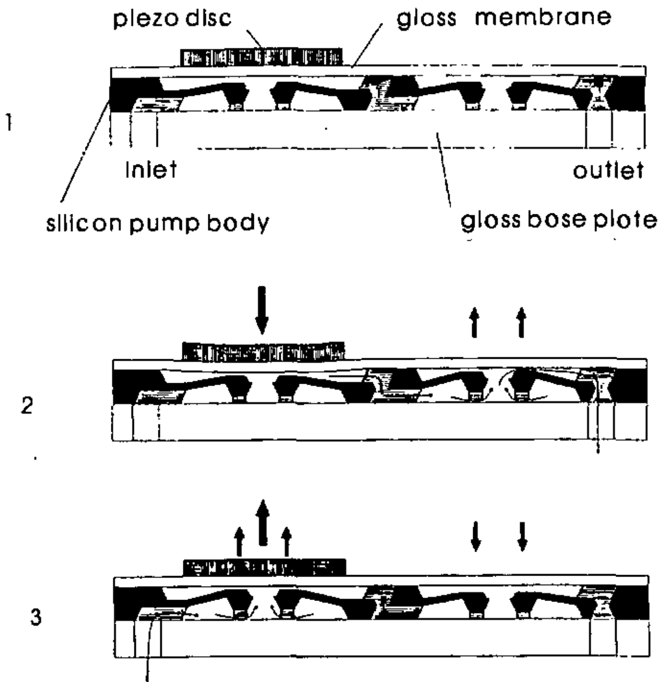

Fig. 15. Operating principle of the piezoelectric micropump [24].

3.3. Mach-Zehnder interferometer sensors

3.3.1. Principle of the Mach-Zehnder sensor

In the Mach-Zehnder interferometer, the light path is split into two separate arms and then recombined [25], [26] . If both interferometer arms exhibit the same length and phase velocity, the guided light will show constructive interference after recombination. Every effect changing the optical path length in one of the interferometer arms, leading to a phase shift of the respective guided wave, then changes the intensity of the emerging wave resulting from the interference [17].

In an integrated optical realization of the Mach-Zehnder interferometer as demonstrated in [27], the light is guided in stripe waveguides, the beamsplitters being replaced by Y-couplers (cf. Fig. 16). The evanescent field of the stripe waveguide forming one of the interferometer arms is influenced by the test substance acting as the cover medium of the

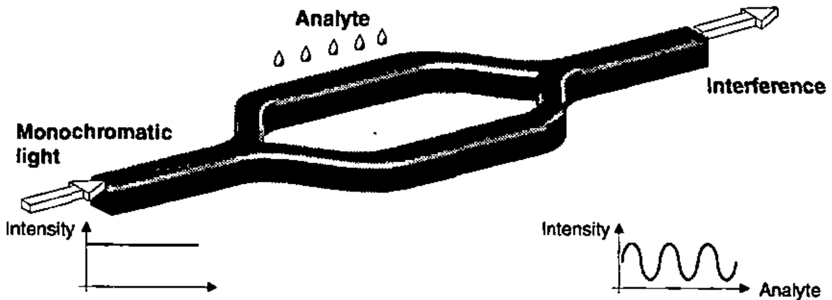

Fig. 16. Function principle of the integrated optical Mach-Zehnder sensor.

waveguide, thus changing the phase velocity. A change of the refractive index of the cover medium can then be determined from the interference signal at the output. An advantage of this interferometric sensor compared to the sensor based on grating coupler resonance is the potentially long

interaction length of the test substance with the waveguide; it is in principle only limited by the sensor size, in practise also by the waveguide losses.
To enable precise measurements, the stripe waveguides only should guide a single-mode, thus avoiding mode dispersion which distorts the interference signal. This requires a width of the waveguide stripes in the range of some micrometers. To avoid the necessity for photolithographic steps on each sample for the definition of the channel pattern, a method using replication techniques as the only patterning step is highly desirable [28,29]. Following the formation of a surface relief, a hard dielectric film with a high refractive index is deposited over the whole area to form the waveguide [30].

3.3.2.The stripe waveguide

3.3.2.1. Stripe waveguide fundamentals

In a stripe waveguide, the guided wave is not only confined to the core layer in one dimension as in the slab waveguide described in chapter 3.1.1, but is also confined laterally. This avoids spreading of the mode due to diffraction effects and allows a precise control of the light path.
The calculation of the waveguide modes is much more challenging than for the slab waveguide. The modes are not purely TE or TM modes, but so-called hybrid modes, having longitudinal components of both fields. Various methods exist to calculate the resulting field approximately. A very efficient method for calculating the field distributions is the "Method of Lines" [31], for which a Computer code exists at the Paul Scherrer Institute. The field arrangements shown in the next chapter were evaluated with this method.

3.3.2.2. Waveguide concept and arrangement

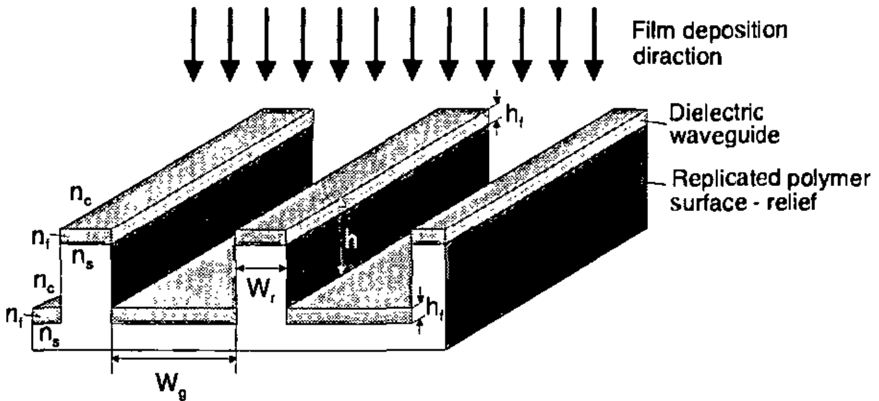

Fig. 17. Stripe waveguide concept : fabrication by embossing and large-area deposition of dielectric.

The approach for the stripe waveguides is based on a concept proposed in reference [30]. Ridge waveguide structures are defined in the substrate material by hot embossing followed by coating the whole chip with a high-index film, which acts as the core of the waveguide. Since an anisotropic deposition process is employed and the height of the ridge structures is chosen much larger than the film thickness, the film is deposited primarily on top of the ridges and at the bottom of the embossed grooves (see Fig. 17). Both the film on top of the ridges as well as the film in the grooves act as stripe waveguides of widths W_r and W_g, respectively, if the groove depth h is chosen sufficiently large as to avoid mode coupling between the two waveguide types. In [30], the beat length of a directional coupler consisting of two vertically separated Ta_2O_5 waveguides on a polycarbonate substrate was considered as a function of the distances between the waveguides. It was expected from the results in this paper that a ridge height $h \approx 3$ μm is sufficient to optically decouple adjacent groove- and ridge-type waveguides. It was then experimentally shown (cf. Chapter 5) that this dimension also leads to efficient decoupling of waveguides formed of TiO_2 on quartz and TiO_2 , TiO_2/SiO_2 and Si_3N_4 waveguiding films on polycarbonate.

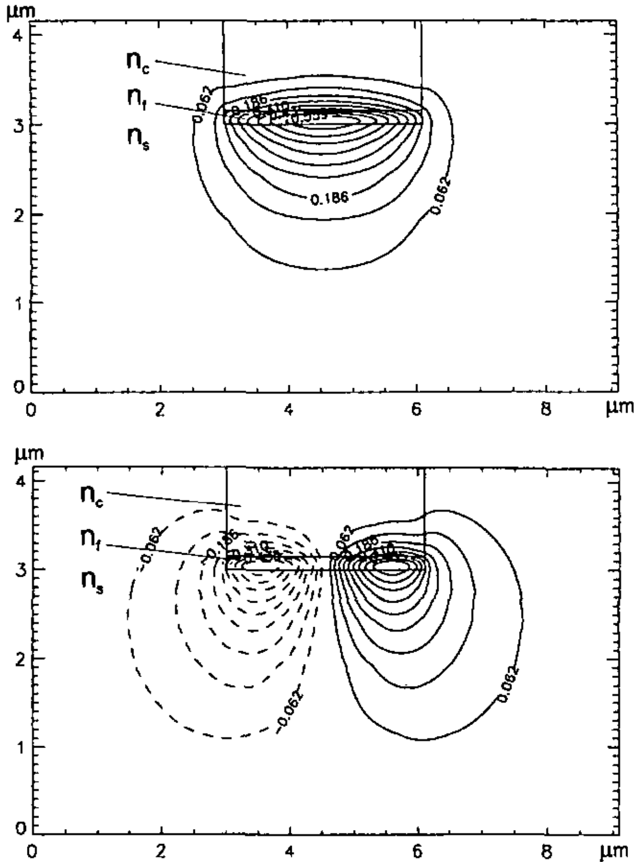

Fig. 18. Electrical field distribution contours of a stripe waveguide calculated using the Method of Lines.

To prevent the edges of the ridge structure from also being coated with the high-index film, they have to be very steep. Additionally, the use of high-index films implements high scattering losses at imperfections of the waveguide surface and edges. The technique employed to achieve steep and smooth edges is described in Chapter 4.3.2. Due to the fact that the roughness of the waveguide edges is higher than the surface roughness, it is favourable to keep the index variations on the edges as low as possible. If the cover substance shows a lower refractive index n_c than the substrate

index n_s , the 'groove-type' waveguide is preferable, since the waveguiding film is laterally embedded into the substrate. For $n_c > n_s$ the 'ridge-type' waveguide might be better suited, if no additional scattering occurs due to index variations of the cover substance.

Ridge widths in the range of a few microns are required for single-mode operation of the waveguide. Fig. 18 shows the electrical field distributions of the fundamental TM_0 mode and a TM -mode of higher lateral order for a 3.1 μm wide groove-type stripe waveguide. The calculation was performed by the simulation program mentioned in the previous chapter. The waveguide is formed of a 219 nm thick TiO_2 / SiO_2 mixed oxide film with SiO_2 cover on a polycarbonate substrate. At a wavelength of $\lambda = 785$ nm, the width of the waveguide is close to cutoff for the higher order mode. At a width of 3.0 μm, only the fundamental mode is guided.

For testing purposes, stripe waveguides of the described type were realized on quartz substrates and polycarbonate substrates with widths ranging from 1.5 to 8 μm.

3.3.3. Focusing grating couplers

By shaping the grating lines adequately, the light diffracted from a grating coupler can form a focus in free space or in the waveguide [43]. The shape

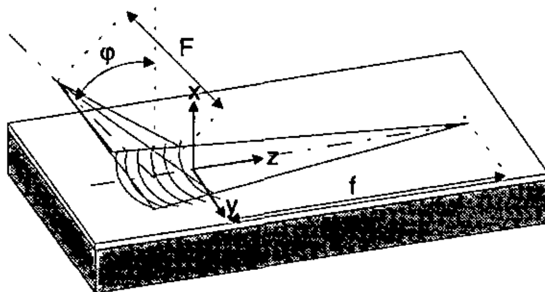

Fig. 19. Scheme of a focusing grating coupler.

of the grating lines can be calculated by a geometric optics approach requiring zero phase difference along the optical path from any point on the wavefront of the incident beam to the focal point in the waveguide. The necessary phase shift, which has to be provided locally by the grating structure, then defines the grating lines. For the general case of coupling light from a focus in free space to a focus in the slab waveguide, (see Fig. 19), the equation for zero phase difference is [32]

$$N \cdot \sqrt{x^2 + (y+f)^2} + \sqrt{x^2 + (y - F \cdot \sin\varphi)^2 + (F \cdot \cos\varphi)^2} = N \cdot f + F + m \cdot \lambda \tag{24}$$

where the effective refractive index of the waveguide is denoted by N, the focal length of the grating in free space by f, the focal length in the waveguide by r, the input angle by φ and the free space wavelength by λ. Solving equation (24) for the coordinates x and y leads to the curve of 4th order given by the formula

$$x^4 + 2x^2 \cdot (y^2 + a_1 y + a_2) + (y^4 + b_1 y^3 + b_2 y^2 + b_3 y + b_4) = 0 \tag{25}$$

with the parameters

$$a_1 = 2 \cdot \frac{N^2 f + F \cdot \sin\varphi}{N^2 - 1} \tag{26}$$

$$a_2 = -\frac{(N^2+1)\cdot(2NfF + 2Nf\lambda m + 2\lambda mF + \lambda^2 m^2) + 2N^2 \cdot (f^2 + F^2)}{(N^2-1)^2} \tag{27}$$

$$b_1 = 4 \cdot \frac{N^2 f + F \cdot \sin\varphi}{N^2 - 1} \tag{28}$$

$$b_2 = -2 \cdot \left(\frac{2N^2 \cdot (f^2 + F^2 - 4fF \cdot \sin\varphi)}{(N^2-1)^2} + \frac{(N^2+1)\cdot(2NfF + 2Nfm\lambda + 2Fm\lambda + m^2\lambda^2) - (N^2 f - F \cdot \sin\varphi)^2}{(N^2-1)^2}\right) \tag{29}$$

$$b_3 = -4 \cdot \frac{2N^2 fF \cdot (F - f \cdot \sin\varphi)}{(N^2-1)^2} + \frac{(N^2 f - F \cdot \sin\varphi) \cdot (2NfF + 2Nfm\lambda + 2Fm\lambda + m^2\lambda^2)}{(N^2-1)^2} \tag{30}$$

$$b_4 = \frac{m\lambda \cdot (2F + m\lambda) \cdot (2fN + m\lambda) \cdot (2F + 2fN + m\lambda)}{(N^2-1)^2} \tag{31}$$

By calculating the grating lines using these formulas, a grating can be designed coupling the light of a laser diode -which can be seen as a point source- to a focused mode in the waveguide without any additional optical elements. To achieve optimum coupling conditions, the input beam has to be adjusted to the design parameters in five degrees of freedom : the angle φ, the lateral tilt angle ψ and the three cartesian coordinates x, y and z.

To ease optical alignment in the test phase, the gratings on the test samples were designed to couple a focused waveguide mode to a collimated free-space beam. This setup is of course insensitive to a displacement along the axis of the input beam and only slightly sensitive to a lateral displacement of the beam. Thus, the adjustment of critical parameters was reduced to the input angles φ and the lateral tilt angle ψ.

For the special case of coupling a collimated free-space beam at an input angle φ to a focus in the waveguide, the mth grating line of a grating for diffraction in the first order is given by

$$N \cdot \sqrt{y^2 + (f - z)^2} + z \cdot \sin\varphi = N \cdot f + m \cdot \lambda \tag{32}$$

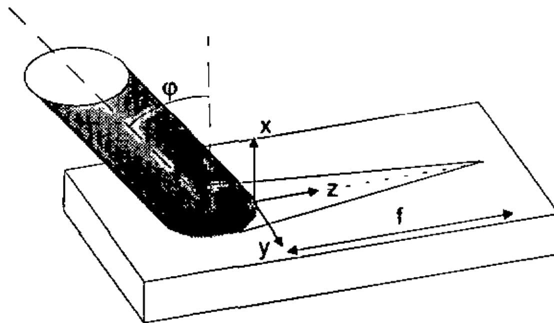

Fig. 20. Schematic diagram of a collimated free space beam coupled to a focused waveguide mode.

(see Fig. 20). Solving this equation for the coordinates y and z yields grating lines analytically described by an ellipse equation, the parameters of each line being defined by the integer index m.

For the fabrication of the grating structures employed in this work at the Swiss Center for Electrotechnic and Microtechniques (CSEM), the calculated parameters of the grating lines had to be converted into the format of the program MENTOR, which is usually employed at CSEM for calculating diffractive optical elements (DOEs). It was thus possible to reduce the data submitted to the system to four parameters instead of an extremely large bitmap :
(1.2 *mm* field length / 25 nm grid size)^2 = 2.3*10^9 data points = 2.1 Gbit, which is impossible to handle for the system.

3.3.4. Concept and design of the IO interferometer sensor

The coupling of light into the waveguide is most conveniently achieved by a grating coupler, thus avoiding problems with end-face preparation of the chips [14]. The fabrication of grating couplers in waveguides by embossing was demonstrated in [33] the fabrication by photopolymerization of linear grating couplers [34] and grating couplers designed to form a focus in free space as well as stripe waveguides in [35]. If the grating is designed to focus light from an external source into the stripe waveguide on chip, the requirements for external optics are strongly reduced.

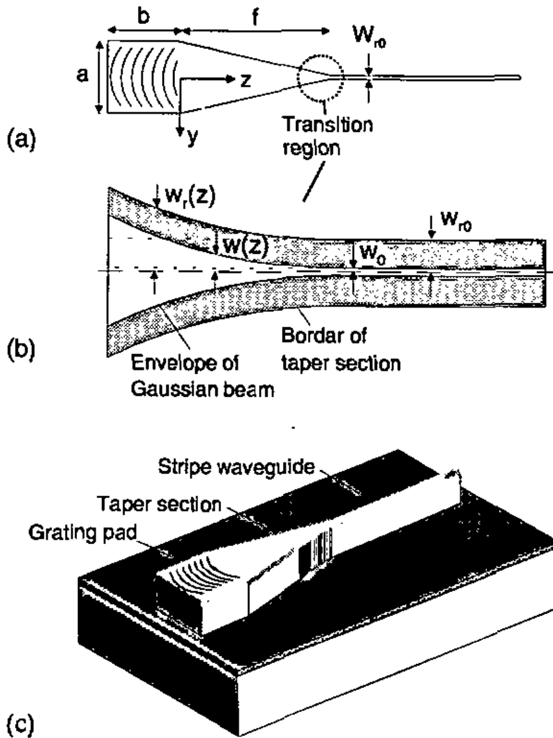

Fig. 21. (a) Configuration of the grating pad, taper section and stripe waveguide, (b) detail of the transition region, (c) schematic view of the structure.

To ease the external alignment, the grating in the realized device was designed to couple a collimated free-space laser beam into a focus within the waveguide, as described in the previous chapter. The depth of the grating structure has to be in the order of 10 nm for the high-index waveguides employed [3].

The lateral intensity distribution of the mode focused in the slab waveguide can be described by a Gaussian beam approximation [36], the beam (half-) width being given by

$$w(z) = w_0 \cdot \sqrt{1 + \left(\frac{\lambda \cdot (f - z)}{N \cdot \pi \cdot w_0^2} \right)^2} \tag{33}$$

where w_0 denotes the beam waist in the focal point (see Fig. 21a and b). The light coupled in by the grating is first focused in a planar section of the waveguide. Instead of simply placing a straight channel guide with its end face into the focal region, the channel guide is connected to the focused mode via a width-tapered transition region, thus minimizing light scattering at the entrance of the channel guide. The shape of the taper was adapted to the envelope of a focused Gaussian beam by choosing its outline half-width $w_r(z)$ corresponding to the formula

$$w_r(z) - w_{r0} = S \cdot \left(w(z) - w_0 \right) \tag{34}$$

where $w_{r0} = W_{r0}/2$ denotes the half-width of the stripe waveguide and S is a scaling factor chosen to adapt the taper to the corresponding stripe waveguide width (see Fig. 21b). The scaling according to Equation (34) provides a smooth transition from the planar section to the channel guide. Most of the waveguide section connecting the grating pad to the channel guide has a straight boundary, except for the transition region next to the entrance face of the straight waveguide. This corresponds to the far and near field regions of the Gaussian beam, to which the width taper was adapted.

Fig. 21c schematically shows the combination of grating pad, taper section and stripe waveguide. In the device realized, this structure is surrounded by a groove with a width $W_g = 100\ \mu m$. This width was arbitrarily chosen for a good decoupling from adjacent on-chip IO components.
Based on this operating principle, a Mach-Zehnder interferometer can be fabricated incorporating input and output grating coupler pads to achieve convenient coupling to the structure (see Fig. 22).

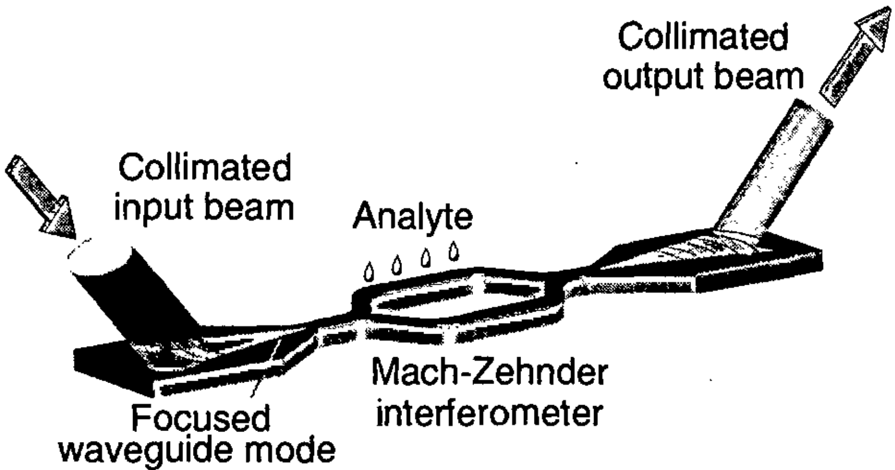

Fig. 22. Integrated-optical Mach-Zehnder interferometer sensor with focusing grating couplers for light input and output.

Identical pads were used for input and output of the light beams due to the ease of fabrication and to achieve high flexibility with choosing the pads for input or output. It is well known that a free-space beam emerging from a waveguide via a grating coupler usually does not show a Gaussian intensity distribution [37]. This can be circumvented by varying the grating depth along the grating [38] to achieve a locally adapted grating efficiency, leading to a Gaussian output beam.

In the test sample, focusing gratings were designed for the wavelengths 633 nm (red HeNe laser) and 785 nm (infrared laser diode), an input angle $\phi = 15°$ and a focal length f =2.5 mm. The beam waist in the focal point was

designed to be $w_0 = 1.0$ µm for $\lambda = 633$ nm and $w_0 = 1.3$ µm for $\lambda = 785$ nm, for illumination producing a $1/e^2$ intensity halfwidth $w(0) = 300$ µm at the grating pad boundary. The size of the pad was designed to be about twice the beam diameter, leading to the dimensions $a = b = 1.2$ mm. Additionally, linear grating couplers were implemented for test purposes.

The stripe waveguides on the test sample had a width ranging from 1.5 µm to 6 µm. For every waveguide width, a long stripe of 12 mm length and two short stripes of 1.8 mm length were implemented. This complete pattern was realized twice, each half being equipped with the focusing grating couplers for the respective wavelength.

Similarly, short and long Mach-Zehnder interferometers equipped with the gratings for both wavelengths were realized on the test sample.

3.3.5. Passivation and sealing layers

For applying the replicated Mach-Zehnder devicc as a sensor, part of the structure has to be protected against the influence of the measurand. The necessity for passivating one of the interferometer arms could be avoided by choosing different arm lengths leading to different phase shifts under influence of the measurand, as demonstrated for an integrated-optical temperature sensor in [39]. However, the input and output grating pads have to be protected, since a change in the effective index in the grating region degrades the coupling efficiency from the free-space beam to the stripe waveguide. This effect would -for small index changes- superpose the intensity modulation caused by the interference or -for large index changes- make the coupling to the stripe waveguide impossible.

The passivation film has to be of good optical quality, since it forms the covcr medium of the waveguide. SiO_2 layers, which are widely used as electrical passivation layers in chip fabrication, can be coated with high quality by Plasma-enhanced vapour deposition (PECVD), evcn at the low temperatures necessary for the polymer substrates. The window for the sensing region can not be opened by an etching technique, since this could damage the waveguiding film. A liftoff technique [40], wherc the SiO_2 layer

is partly coated onto a photoresist pattern, which is subsequently resolved, removing the cover layer at this location, has to be performed carefully. The solvents for removing the resist, acetone or Photoresist Remover[5] attack the polycarbonate substrate, leading to an opaque white surface. Tests performed with coating the backside of the sample with a 50 nm SiO_2 film before performing the liftoff step improved the situation, however, damages of the substrate still were visible. It can be concluded that the waveguiding film and the protection layer on the rear side need to be almost pinhole-free to make a liftoff-technique on the polymer samples applicable.

[5] Microposit 1165 Remover

4. Fabrication of the components

In this section, the fabrication methods for the different integrated optical structures used in the thesis are described. The common fabrication principle of all integrated optical devices employed is to produce a surface relief in a planar substrate, followed by coating the whole surface with a high-index waveguiding film. While the coating process generally can be performed on a large number of samples simultaneously, the method for the fabrication of the surface relief mainly determines the effort for manufacturing the integrated optical structure.

4.1. Substrate patterning techniques

The most common method for producing well-defined surface relieves in a planar substrate is to first generate the desired pattern in a photoresist layer and to transfer it into the sample in a subsequent step [40]. The photoresist layer can be deposited directly on the chip, the pattern transfer into the substrate being achieved by an etching technique; or the surface relief is first transferred onto an intermediate structure, which is mechanically and chemically more stable than the resist pattern. If a polymer is used as substrate material, structuring of the sample surface then can be performed by a replication technique, such as hot embossing or injection molding [41, 42]. Whereas the direct patterning technique requires a photolithographic step followed by etching on each sample, the patterning of the samples by replication techniques offers the possibility of low-cost mass production.

4.2. Grating Coupler fabrication

4.2.1. Linear grating couplers

Various types of grating couplers were employed for the different sensor schemes. For the sensors based on the integrated optical light pointer principle, linear gratings in thickness-tapered waveguides and chirped gratings in homogeneous waveguides were employed. For the excitation of modes in channel waveguides, focusing grating couplers were applied.

The process of the linear grating fabrication established at the Paul Scherrer Institute is described in detail in [3]. Therefore, only a brief description of the technique will be given. The fabrication of the linear grating couplers starts with coating a quartz substrate with an anti-reflection layer[6] and a photoresist film[7]. The sample is then exposed by laser interference (holographic exposure) of a HeCd laser operating at a wavelength of $\lambda = 442$ nm. After development, a sine-shaped grating pattern in the resist is obtained. The sample then is placed into an e-beam evaporation system equipped with a chromium target and mounted with a tilt angle (about 10°), so that the anisotropic deposition process leads to covering only the top parts of the grating pattern with chromium ('shadow evaporation'). These metal caps serve as a mask in a subsequent oxygen reactive ion etching (RIE) step, so that the shallow grating is transferred deeply into the resist layer, featuring very steep sidewalls of the grating lines, and further into the quartz substrate. After stripping, a grating with almost rectangular profile is obtained.

The necessary depth of the grating couplers for best coupling conditions depends on the specific dimensions and refractive indices of the substrate, waveguiding film and cover medium. For the high-index waveguides on low-index substrates employed in this work, the optimum grating depth generally was in the range of about 5 to 25 nm. To produce these shallow corrugations in a quartz substrate, an oxygen RIE system[8] was used for the pattern transfer. Since laser end-point monitoring is not applicable at those

[6] Brewer ARC-XLT
[7] Shipley AZ1400-17
[8] Oxford Plasmalab 80 Plus

very low etching depths, this system has the advantage of a very low etching speed (~ 0.7 nm/min at the standard process parameters[9]), so that the etching depth can conveniently be controlled by the etching time. The use of more reactive etching gases - as for instance CHF_3 - would reduce the etching time to the range of seconds, making a precise control difficult. The required time for etching to the desired depth was determined by performing atomic force microscope measurements of etched test samples.

4.2.2. Chirped and focusing grating couplers

Although more complicated grating structures such as focusing grating couplers can also be fabricated by interferometric exposure techniques [43,44], considerable optical aberrations occur due to the different wavelengths for exposing the grating pattern and for coupling to the waveguide [45]. Theoretically aberration-free structures can be realized by direct electron-beam (e-beam) writing techniques as first demonstrated in [46].

The e-beam writing steps for the samples used in this thesis were performed by the Swiss center for electrotechnics and microtechnique (CSEM) on a commercial e-beam system[10]. For this technique, a chromium-coated (layer thickness ~80 nm) quartz plate is coated with e-beam resist, in most cases a 200-300 nm thick layer of polymethylmethacrylate (PMMA). This sample is loaded into the e-beam system onto a xy-stage, which is used to move the sample under the e-beam source. The electrons in the system are emitted by a heated LaB_6 (Lanthanum-hexaborate) crystal, accelerated by a voltage of 20 kV or 50 kV and bundled by a magnetic field to a spot diameter adjustable from 30 to 800 nm. The electron beam irradiating the sample can be deflected by electrostatic fields, enabling an e-beam scan on the sample in a field of 400 x 400 μm size, writing on an address grid of 25 nm, without moving the xy-stage. For writing a larger area, the xy-stage is moved to the next writing field. In the system employed at CSEM, structures with dimensions of 5" x 5" can be processed this way. After development, the pattern is transferred into the chromium layer by an RIE step using a chlorine-based process gas. This procedure is usually employed for the

[9] 80 W, 20 sccm O_2, 5 mTorr
[10] Leica EBPG-3 (Electron Beam Pattern Generator)

fabrication of photolithographic masks for the semiconductor production, but also can be applied for the fabrication of very fine grating structures. The grating pattern was then transferred into the quartz substrate by an RIE step using oxygen as process gas, as described in the previous chapter.
Fig. 23 shows an Atomic Force Microscope (AFM) image of a section of a focusing grating coupler pattern without waveguiding film fabricated by the process described above. The grating period is 462 nm, the measured grating depth is 6.1 nm. The average (RMS) roughness of the structure is 1.5 nm, mainly due to residues of the process of chromium removal.

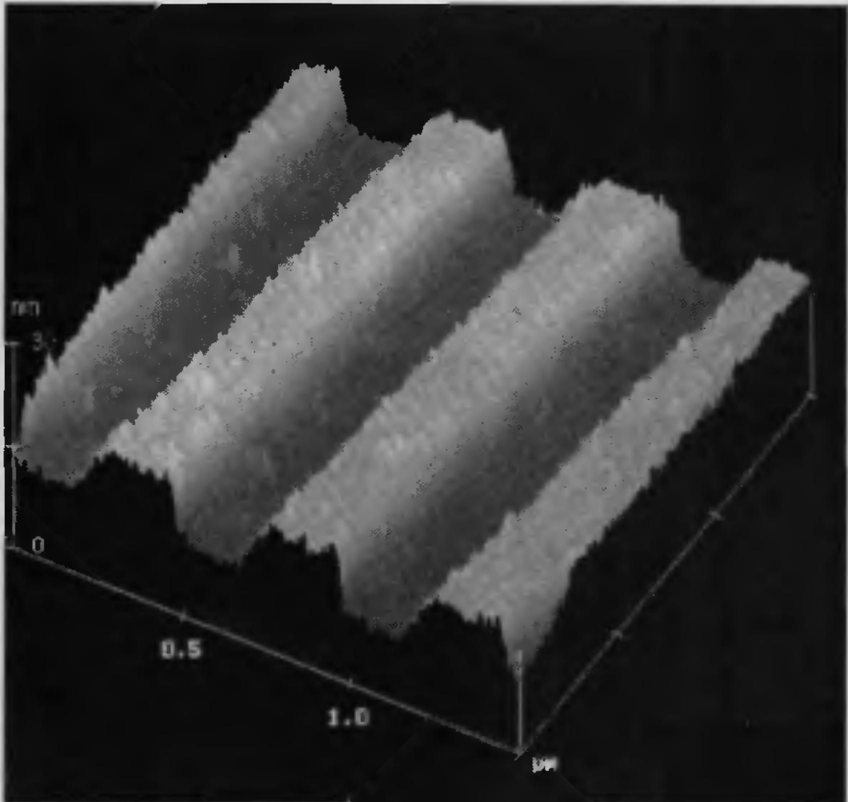

Fig. 23. AFM measurement of a focusing grating profile etched into a quartz substrate.

4.3. Fabrication of stripe waveguides and interferometer structures

4.3.1. Fabrication steps

The pattern transfer by UV-exposure of a planar photoresist layer through a photomask is the most widely used technique in micoelectronics [40]. This method was used for the fabrication of the waveguide structures. In Fig. 24 the main fabrication steps are outlined. After transferring the waveguide pattern into a relief in photoresist (see next chapter), the substrate is patterned by RIE (see Chapter 4.3.3). This sample then serves as a 'master structure', which is electroplated with a nickel layer that is subsequently used for embossing into a polycarbonate foil. On the structured polymer surface relief, the waveguides are formed by coating the complete structure with a waveguiding film (cf. Chapter 3.3.4).

4.3.2. Patterning of photoresist

In the first experiments, a chromium-coated quartz plate was spin-coated with a 1.8 μm thick photoresist layer[11] , into which a stripe waveguide structure was exposed using a conventional Mask Aligner. After development[12] and etching of the chromium layer by a Cerium-bisulfate solution[13] [47], the structure was transferred into the quartz substrate by RIE. Characterization in a Scanning Electron Microscope (SEM) showed that the tilt angle (≈ 15°) of the sidewalls of the resist structure had been transferred almost identical into the sidewalls of the etched pattern in quartz, despite of the different etch rates. This indicated the necessity of producing steeper sidewalls of the resist pattern.

[11] Shipley Microposit 1818 Resist

[12] Shipley MF 319 Developer

[13] 1 g $Ce(SO_4)_2$ $2(NH_4)_2$ $2H_2O$, 5 ml HNO_3 , 25 ml H_2O , 28°C

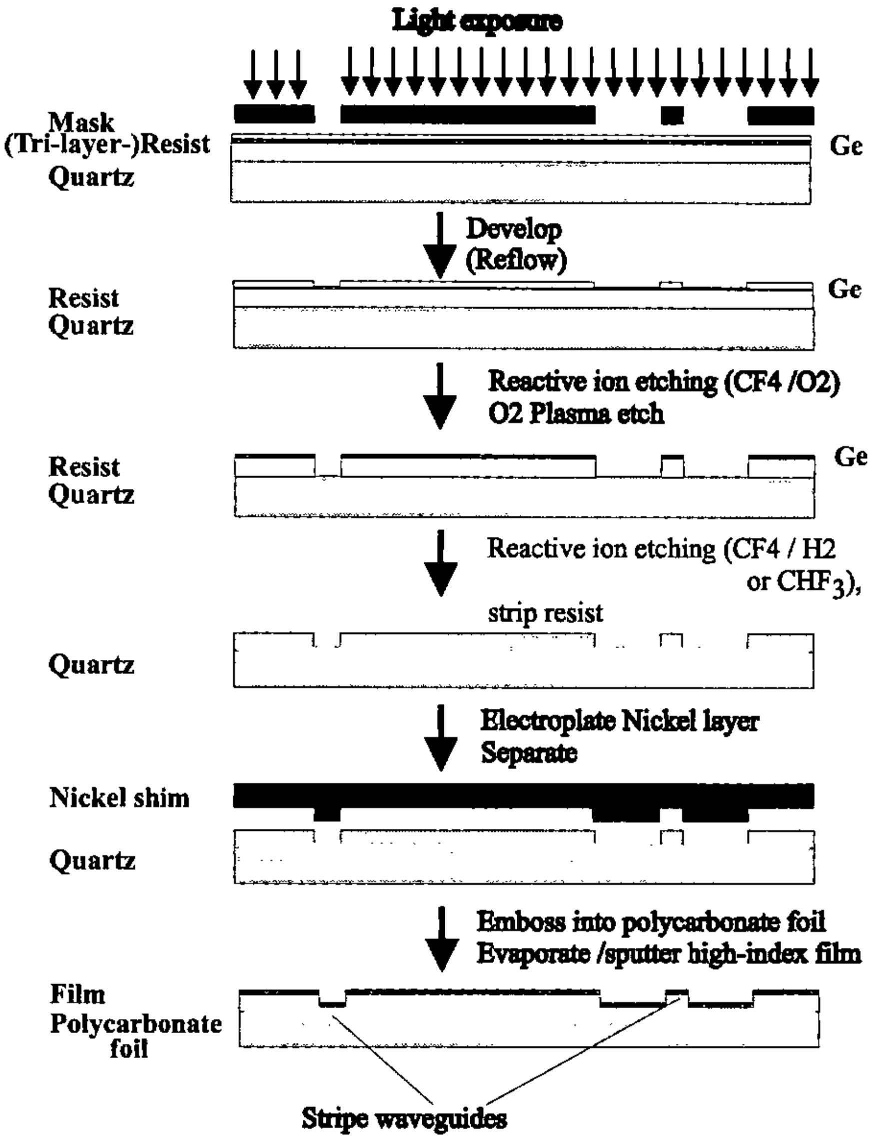

Fig. 24. Schematic display of the fabrication steps for producing the stripe waveguide structures.

The steepness of the sidewalls can easily be increased by reducing the thickness of the resist layer. This method is limited, however, by the selectivity of the etching process. A tri-layer technique [48] combines the high quality of pattern transfer into a thin resist layer with the advantages of a thick resist layer in the etching process. In the test samples, a thick (1.8 μm) resist layer is spin-coated onto a chromium-coated quartz plate and then baked on a hotplate at 140°C for 10 minutes to completely remove the solvent from the film. Subsequently, a germanium film of 40 nm thickness is formed on the resist by e-beam evaporation, which is then coated with a thin (500 nm) resist layer. The waveguide pattern is exposed into this layer. After development, the pattern is transferred into the germanium layer by RIE using CF_4 and O_2 as process gases. The metal serves as a mask for the subsequent O_2 RIE step, this process being performed at low pressure (~ 5 mTorr) to achieve very anisotropic etching (cf. Fig. 24). The structure formed in the thick resist layer now can be used for masking in the further process steps like the directly exposed resist structure, while showing a higher thermal stability in the etching process due to the bake performed on this layer. Fig. 25 shows Scanning Electron Microscope (SEM) micrographs of the resist patterns resulting from direct exposure and application of the tri-layer technique for the same 2 μm wide stripe structure.

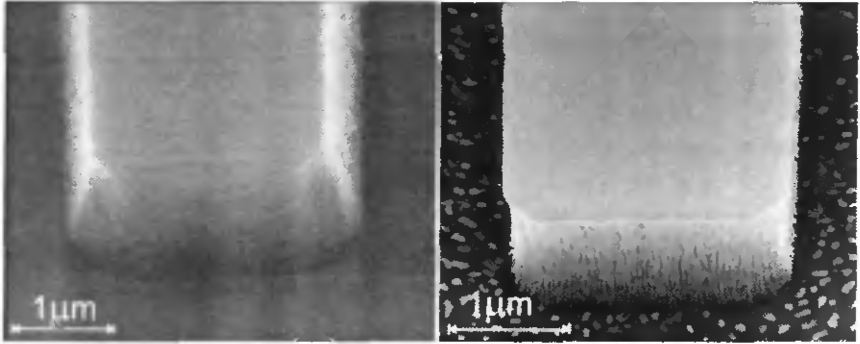

Fig. 25. SEM micrographs of resist patterns obtained by direct exposure (left) and tri-layer technique (right).

To obtain smooth sidewalls of the stripe waveguides, a postbake was performed on the structured photoresist leading to a thermal reflow of the structure [49]. It is an advantage of the tri-level process, that the reflow can be done with the structures in the upper resist layer, so that the steepness of the resulting resist sidewalls is not degraded. In Fig. 26, the resist structure for a y-junction is depicted. The left figure shows the upper resist layer after the postbake step[14], the right picture shows the lower resist layer after etching the chromium film. The substance deposited on top of the resist is a residue of the wet etching step.

It is mandatory to perform the reflow step immediately after structuring the upper resist layer, because water absorbed in the lower resist layer destroys the germanium film during the heating process.

[14] 140°C, 10 minutes.

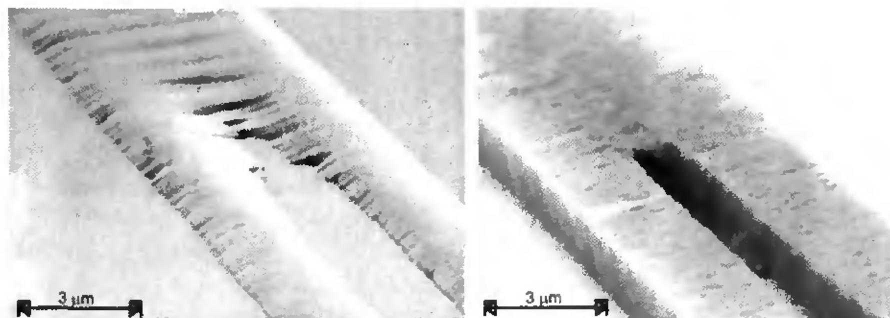

Fig. 26. SEM micrograph of a y-junction in photoresist :
Left : Upper layer after thermal reflow, right : pattern transferred to lower resist layer.

4.3.3. RIE of Quartz

The transfer of the waveguide pattern into the quartz substrate was done by reactive ion etching (RIE) [50]. An etching depth of about 3 µm had to be achieved to avoid strong mode coupling between the channel waveguides and the slab waveguide [30]. Since experiments had shown that the shape of the resist profile had a strong influence on the profile of the etched structure, a resist pattern with steep and smooth sidewalls had to be produced to achieve the same quality in the pattern in SiO_2 (cf. Chapter 4.3.2).
Two RIE systems with different sets of process gases were tested for best etching results. Either CHF_3 or a mixture of Freon (CF_4) and Hydrogen were employed as etching gases. The main process requirements were

i) high anisotropy of the etching process leading to steep sidewalls,
ii) good selectivity of the process concerning the etch speed of the SiO_2 in comparison with that of the resist mask,
iii) low roughness of the etched sidewalls.

Generally, etching gases containing fluorine, carbon and hydrogen tend to the formation of polymer films in the reaction chamber [50], which can lead to masking effects that disturb the homogeneity of the etching process. The

process parameters used for the fabrication were a tradeoff between selectivity and polymer formation. The required anisotropy of the etching process requires low pressures, but this reduces the etching speed.

A commercial RIE system was employed to perform etchings of quartz by a mixture of CF_4 and H_2. In [51], this set of process gases was investigated with a focus on the avoidance of polymer formation in the reaction chamber. However, the parameters given for a specific reactor usually are not transferrable to other systems. For this reason, various etching tests were performed to optimize the process parameters

To optimize the process parameters with respect to etching selectivity and speed, a number of test samples were fabricated and processed. These were pieces of 10 x 10 mm size consisting of a thermally oxidized Si wafer (oxide thickness ~2 nm) with a resist film of 1.8 μm thickness, in which a relatively coarse grating of 160 μm period was exposed and developed. The grating served as a convenient pattern to measure the structure depth with a stylus profilometer. By performing this measurement before and after the etching process and after stripping the resist, the etching speed in the SiO_2 and in the resist film and hence the selectivity of the process was determined.

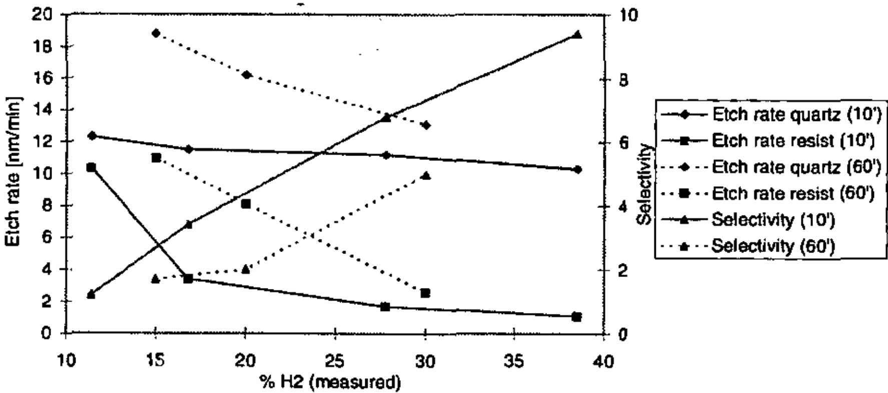

Fig. 27. Etch rates and selectivity of RIE on quartz using CF4 and H2 as process gases. Etching time : straight line 10' / dotted line 60'.

In Fig. 27 the etching speed of the resist and thc SiO_2 are depicted for different H_2 contents in the process gas while keeping the total flow rate constant at 50 sccm. The Power was 100 W and the pressure was 15 mTorr for this process series. It can be seen clearly, that the ctch rates for both the resist and the quartz decrcase with increasing H_2 content. But as the etch rate of the resist decreases more rapidly, the selectivity increases with higher H_2 contents in the etching gas. Selectivities of up to 10 were achieved for short etching times, but already with some amount of polymer formation on the sample, leading to inhomogeneous etchings. Two series of etching tests were performed, the first batch being etched for 10 minutes and the second for 60 minutcs. The graph shows that the selectivity decreases significantly with etching time. For an etching depth of 3 μm and an etching rate of about 15 nm / min, the process takes 200 minutes, leading to a further reduction in selectivity. For this reason, the selectivities for the stripe waveguides etchings were around 3 for this system.

The etchings using the CHF_3 as process gas were performed on an in-house built RIE system with manually operated pressure and power control. It was cvaluated that on this system selectivities of 6 to 7 could be achieved without significant amounts of polymer formation on the sample at a pressure of 10 mTorr, flow rate 23 sccm and 80 W RF power. For this reason, the etching processes were shifted to this system.

4.4. Combination of grating and waveguide structure

The combination of the waveguide structure with the grating pattern is shown in Fig. 28. After fabrication of thc focusing grating patterns by e-beam direct writing, the patterns are etched into the chromium layer and subsequently into the quartz substrate. Using the same technique, but without etching to the substrate, a photomask containing the waveguide structure is producod. This mask is then employed to transfer the waveguide

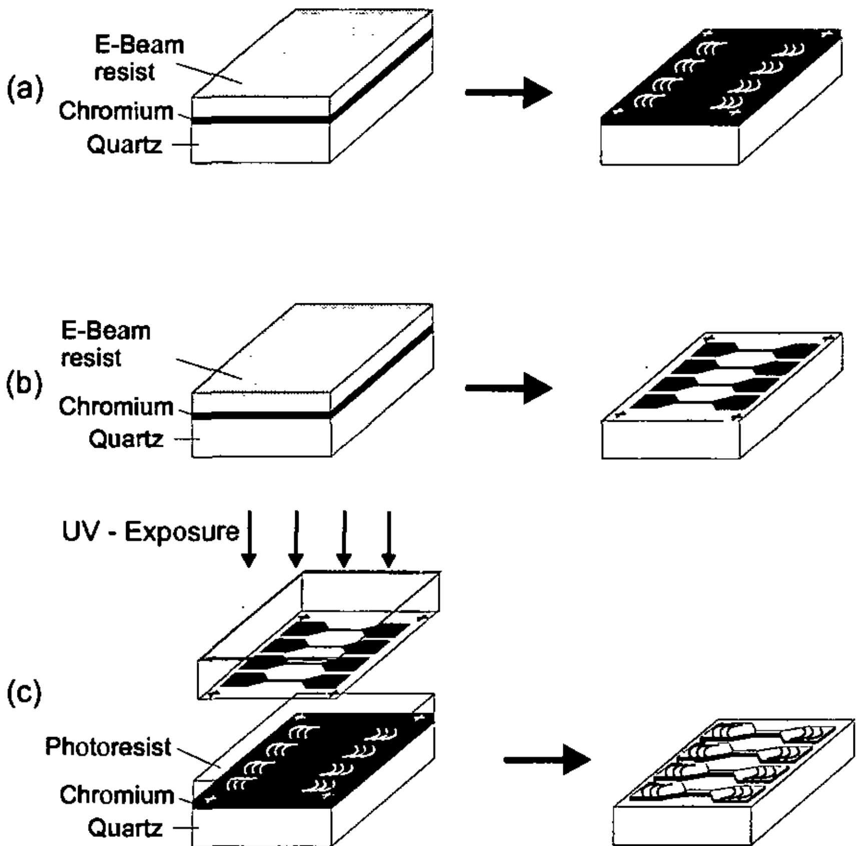

Fig. 28. Fabrication steps for the production of a master sample containing both gratings and waveguide structures.

pattern in a photolithographic step into a photoresist layer coated on the sample with the focusing gratings. Obviously, the alignment of the grating pattern with respect to the waveguide structure has to be very precise ($< 1\ \mu m$) to achieve coincidence of the grating focus and the entrance of the stripe waveguide.
The master sample can be electroplated as shown in Fig. 24 to produce an embossing shim for replication of the structure.

4.5. Replication

The surface relief formed in the master structure can be transferred into a polymer substrate by replication techniques, such as hot embossing or injection molding [42]. Since the quartz substrate itself is not sufficiently stable for the use in the mentioned replication techniques, its surface relief is first transferred to a metal film. This can be obtained with high quality by electroplating the surface with a metal layer. Nickel is mostly used as deposited metal due to its mechanical stability and the rich experience in producing high-quality, stress-free films on the surface of the structure. In a first step, a 100 nm thick gold or silver film is sputtered onto the surface of the master sample to obtain a conducting surface. This process was performed in a commercial sputtering system[15] using Argon at a pressure of 16 μbar as process gas and applying a RF power of 50 W to the chamber, resulting in a deposition rate of 16.5 nm/min.

Then the sample is contacted and placed into a galvanic bath, consisting of a solution of Nickel sulphamate ($Ni(NH_2SO_3)_2$)[16] and Boric acid (H_3BO_3) in water [52]. The electrodes are formed of the contacted substrate itself as the cathode and a metal basket filled with nickel pieces acting as the anode. A current density of $40\ mA/cm^2$ is applied for the process commonly employed in our institute. With this parameters, a nickel film of 250 μm thickness is deposited in about 5 hours. After separating, the shim is cleaned in an Oxygen Plasma Asher to oxidize residual contaminations.

[15] Perkin Elmer Randex Sputtering System, Model 2400
[16] BARRETT Nickel sulfamate concentrate SNR-24

If the surface of the sample is not completely smooth, but contains rougher sections due to the etching process, the process of separating the sample and the shim has to be performed with great care. In one of the samples processed for this thesis, the etched sections of the sample surface consisted of microscopic "needles" formed in the surface of structure. This led to an extremely strong adhesion between sample and shim, which could not be separated without destroying the quartz master. A better choice of the etching parameters leading to smoother surfaces avoided this problem in subsequent processes.

The choice of either gold or silver as starting layer for electroplating depends on the further use of the shim. If it should be employed for producing additional shims in subsequent electroplating steps, the choice of a less noble metal than gold is mandatory to get the possibility of passivating the surface. Otherwise, the two structures can not be separated after electroplating. If the shim is directly used for embossing, coating with gold is preferable due to its high chemical durability.

The hot embossing process is a good method for the replication into polymer materials in small quantities. It is described in detail in [33], where also a theoretical model for describing the shaping process in the polymer surface is given. The principle of the embossing process is to press the hard master structure into the substrate material, which has been softened by heating. Thermoplastics are well suited substrate materials for this process since they show a soft, viscous state in a large temperature range between their glass transition temperature and their melting point. The glass transition point, which can be defined for all polymers, describes a transition from the solid to a viscous state, where the polymer chains show an increased mobility relative to each other.

In all experiments performed in this work, polycarbonate (PC) was used as substrate material due to its high mechanical and thermal stability [53], and well suited optical properties. The glass transition point is about 145°C for the PC [33], which can easily be reached by a hot embossing system. PC foils of 250 μm thickness[17] were used as substrates.

---

[17] Röhm Europlex

The embossings were performed on an in-house built embossing system (see Fig. 29) with pneumatic cylinders as actuators providing a stamper pressure of about 20 bar. The sample is placed on a glass block with the shim on top of it. Then a silicon foil and a glass plate are put on this stack. The whole structure is then placed into the embossing system, where the top platc is heated to about 240°C, and pressure is applied. The usual duration of the embossing process is 4.5 min. After rcmoving the stack from the embossing system, it is cooled by placing two copper blocks of about 4.5 kg weight directly on the shim for about 10 minutes. Then the separation of shim and sample can be performed.

An investigation of the sample temperature during the embossing process

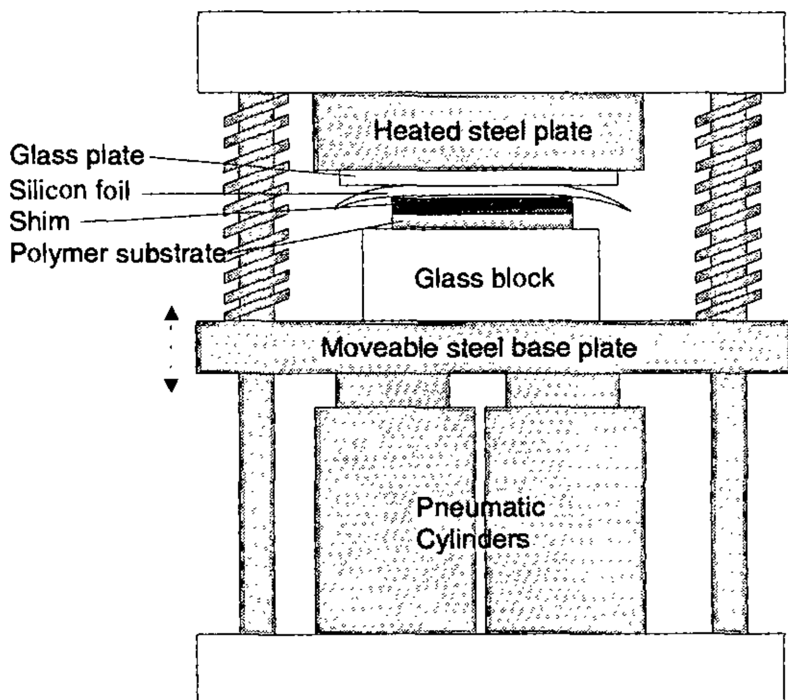

Fig. 29. Scheme of the employed embossing system.

[54] with a heater temperature of 220°C revealed a temperature rise to 175°C in 140 seconds; the glass transition point was reached after 40 seconds. The temperature of the sample was reduced to 100°C in only 30 seconds during the cooling process. The process temperature has to be sufficiently high to reach the viscous state of the polymer in a short time, whereas too high embossing temperatures lead to bubble formation in the sample. The embossing time is not a very critical parameter, but should not be exaggerated due to the reduction of the substrate thickness.

4.6. Film deposition

For the purpose of producing high-index waveguides, different processes for the formation of high-index films on quartz and polymer substrates were developed by Balzers AG, Liechtenstein.

The formation of Ta_2O_5 films on quartz substrates was performed by a "Reactive-low-voltage ion plating" technique [11], by which optical films of excellent quality were generated. Unfortunately, this technique is not applicable on polycarbonate substrates, since the high particle energy damages the polymer surface.

The coating of TiO_2 films also was done by Balzers AG, employing a modified magnetron sputtering process [29, 55]. This technique allows to generate compact high-index films both on quartz and polycarbonate substrates.

Plasma-enhanced chemical vapour deposition (PECVD) is a useful technique to obtain high quality films at relatively low temperatures [55]. Typical process temperatures are in the range of 300°C; it was found in this work that even lower temperatures of about 120°C are applicable to form SiO_2 and Si_3N_4 films on polycarbonate with good quality.

The process is based on starting a glow discharge plasma over the sample in the reaction chamber which is powered by an external RF source. The sample itself is placed on a heated base plate. The high temperature of the electrons in the plasma, usually about 10^4 degrees Kelvin, leads to the formation of reactive species when interacting with the atoms, ions and molecules in the chamber. This allows the use of moderate substrate temperatures for the coating process.

The coatings were performed in a commercial PECVD system supplied by VACUTEC Inc. The process parameters for the formation of Si_3N_4 layers on polycarbonate substrates were :

225 mTorr,
86 sccm of 5% SiH_4 in H_2
147 sccm N_2
100 W

These process parameters led to the formation of a film that was characterized on an ellipsometer. The evaluated refractive index of the film at $\lambda = 633$ nm was 1.86, the deposition rate was 23 nm/min. The refractive index of the film was significantly lower than the value reported in literature [55], but additional measurements performed by B. Maisenhölder at PSI revealed stochiometric composition of the deposited Si_3N_4 film. This led to the conclusion that the film either has some hydrogen content, or it is porous, the pores leading to the decrease in refractive index. If the film is employed for sensing applications, this effect has to be investigated more thoroughly, because the pores might lead to storage effects of the sample solution in the film.

4.7. Deposition of chemically sensitive membranes

The chemically sensitive membranes for integrated-optical chemical measurements were supplied by the Centre for Chemical Sensors, Biosensors and (Bio-)analytical Chemistry, headed by Ms. Dr. Spichiger at the Swiss Federal Institute of Technology in Zurich (ETH Zurich). These substances change their spectral absorption and hence (related by the Kramers-Kronig equations) their refractive index upon a change in the concentration of a chemical substance in the ambient medium. The membranes are solved in Tetrahydrofurane (THF), a highly volatile solvent.

Since the membrane forms the cover layer of the waveguide, it has to be of good optical quality. The deposited solution was filtered to 0.2 μm using teflon membrane filters to avoid scattering at dust and other particles.

Spin coating is a widely used procedure to obtain high-quality films, but the common spin-on procedure for photoresist had to be modified due to the high vapour pressure of the solvent, leading to solidification of the film before the substance had spread uniformly over the surface. In first experiments, a spinner with the chuck placed in a solvent atmosphere was employed, the membrane solution being brought onto the surface by a syringe through a hole in the top of the chamber. The drawback of this setup was an inhomogeinity in the center of the deposited membrane, probably caused by air streams due to the hole in the lid. In a second setup, a spin-chuck suitable for a commercial spinner was constructed. It was equipped with a lid that was placed onto the chuck immediately after depositing the membrane solution onto the sample. Using this device, films of high quality were deposited.

However, optical measurements on planar waveguides consisting of TiO_2 on fused silica showed a highly increased attenuation after deposition of the membranes. This effect could not mainly be caused by scattering, due to the good film quality; and it also occurred with membranes without dyes, thus excluding the effect of optical absorption in the membrane. It was found that by depositing a thin ($\cong 20$ nm) SiO_2 layer by PECVD onto the TiO_2 film before applying the membrane, this effect could be removed. Samples containing this 'barrier layer' showed no apparent degradation after application of the membranes without dye and the absorption expected due to the dye when coated with the measurement membrane.

Since this effect was not observed with waveguides based on Ta_2O_5 films, it might be caused by an interaction between the polyvinylchloride (PVC) that forms the matrix of the sensor membrane and the TiO_2 film. It was already found by other researchers that the direct deposition of TiO_2 onto polycarbonate substrates leads to the formation of an absorbing intermediate layer [56].

5. Component characterization and measurements

5.1. Characterization of the components

5.1.1. Determination of planar and tapered waveguide parameters

To use the waveguide as a sensor chip, the waveguide parameters must be known precisely. The periods of the waveguide gratings were determined by measuring the angles θ of the -1st diffraction order in the Littrow configuration [17], the grating period being given by [3]

$$\Lambda = \frac{\lambda}{2 \cdot \sin \Theta}. \tag{35}$$

Then, different waveguide modes were excited at the same position y_b by adjusting the resonance angles θ_i of the beam illuminating the input grating coupler. In the waveguides used for the measurements, only the TE_0 and TM_0 mode could propagate. The thickness and the refractive index of the waveguiding film at the actual position y_b can be calculated from the resonance angles based on the formulas given in Chapter 3. By repeating this procedure at different waveguide positions y and fitting the evaluated data by a linear model function, the slopes of the waveguide's thickness and index variations are calculated. This measurement was performed at $\lambda = 633$ nm and $\lambda = 785$ nm.

Theoretical expressions derived under the assumption of isotropic dielectric materials in the thin grating limit were used for both characterizing the tapered waveguide and determining the cover refractive index. Therefore, the values hf' for the thickness and nf' for the refractive index are 'equivalent' values corresponding to this approximation [18]. Since the same model was used for determining the gradients $hf'(y)$ and $nf'(y)$ as well as for deriving the cover refractive index, errors resulting from the deviations between the true (hf, nf) and the equivalent values (hf', nf') are kept

negligible if the cover refractive index does not vary in an extremely wide range. Therefore, in order to minimize the error in determining the absolute refractive index, ethanol (instead of air) was used as the reference cover medium for evaluating the spatial refractive index and thickness gradients. For increased precision and a very wide range of refractive indices to be absolutely measured, numerical corrections or a series of calibrating test liquids would have to be applied.

5.1.2. Focusing grating coupler characterization

For testing the FGCs embossed into a planar substrate coated with TiO_2/SiO_2 mixed oxide, a collimated laser beam was directed onto the grating and the light scattered from the focused mode in the slab waveguide was observed by a microscope. Fig. 30 shows a focused TM_0 mode excited by a HeNe laser directed onto a grating coupler of 12 nm depth. In the figure, the light scattered from the structure was intensified by image processing to enable visualizing the focusing characteristics. The resonance angle was 16.4°. The beam waist in the focal point on the waveguide could not be measured directly due to the limited resolution of the microscope image. It was determined by measuring the lateral $1/e^2$-width of the focused beam at

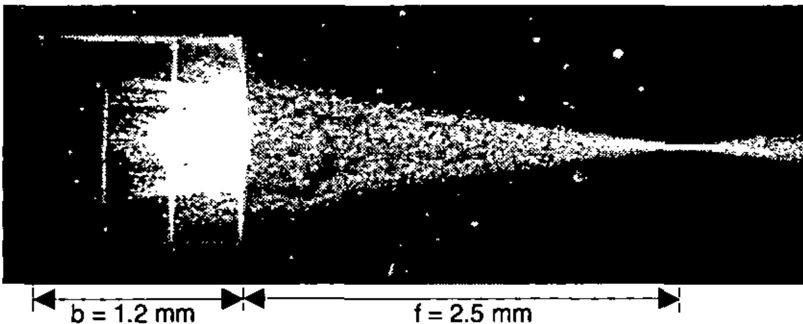

Fig. 30. Focusing grating coupler replicated into a polycarbonate substrate, focusing a TM0 mode.

different z positions between the grating edge and the focal point, and by calculating the beam width in the focal point based on the focusing properties of a Gaussian beam. For the grating shown in Fig. 30, the diameter of the focal spot was determined to be $2w_0 = 3.2\ \mu m$. The two bright vertical lines visible in the grating pad are caused by scattering at the boundaries between the 400 µm x 400 µm scan fields of the e-beam written structure. The film parameters were determined by characterizing a uniform grating coupler substrate coated in the same batch. The effective TM_0 mode indices were $N = 1.641$ at $\lambda = 633$ nm and $N = 1.522$ at $\lambda = 785$ nm, respectively.

Grating depth : 5 nm

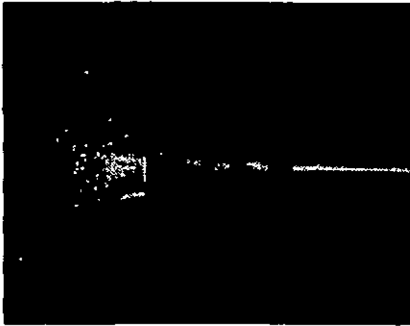

Grating depth : 8 nm

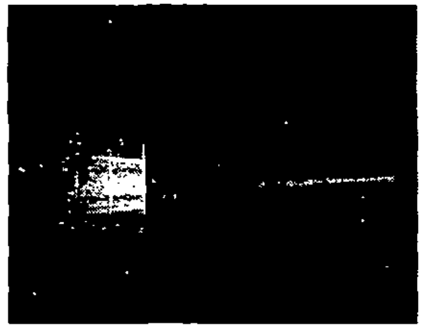

Grating depth : 12 nm

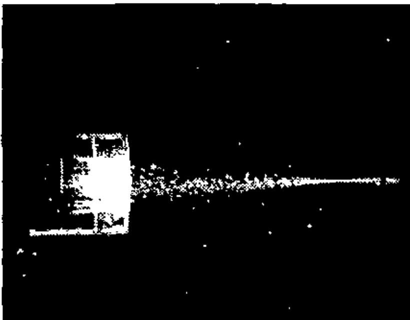

Fig. 31. Influence of grating depth on focused waveguide mode excitation.

Fig. 31 shows focusing grating couplers of different depths embossed into a planar substrate to determine the quality of coupling to the waveguide. The waveguiding film is again a TiO_2 / SiO_2 mixed oxide.

5.1.3. Characterization of stripe waveguides

For characterization of an embossed and coated sample it was placed in a holder incorporating two tension springs to avoid bending of the thin foil. The sample was then mounted on a goniometer table and illuminated by a collimated laser beam. The test sample incorporated waveguides with widths ranging from 1.5 µm to 6 µm and several Mach-Zehnder interferometer structures with a waveguide width of 3 µm.

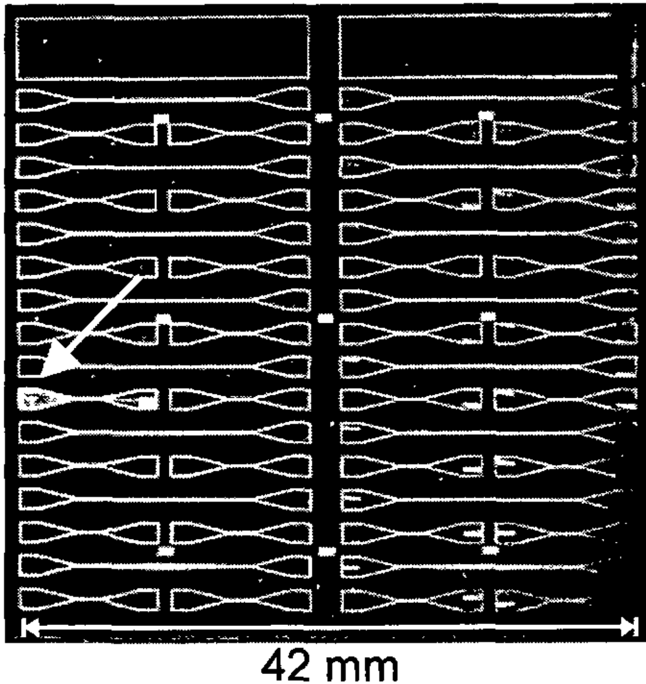

Fig. 32. Photograph of a test sample consisting of a replicated polycarbonate foil coated with a Si_3N_4 film.

In Fig. 32, a photograph of the polycarbonate foil mounted in the holder is shown. The foil was illuminated laterally by a white light source to make the grating couplers visible. The short and long waveguide structures are clearly visible, as well as the different gratings facing toward stripe waveguides or into planar regions. In one of the short waveguide structures, indicated by the arrow, a waveguide mode was excited in a 4 µm wide stripe waveguide by illumination of a grating pad with a red HeNe laser.

The grating couplers and waveguide structures were investigated by adjusting the incident light beam to the resonance angle and observing the light scattered from the excited mode in the planar waveguide and the waveguide stripes by means of a microscope connected to a CCD camera. First, a structured polycarbonate foil coated with a Si_3N_4 film of 260 nm thickness was investigated.
Fig. 33 is a micrograph of a focusing grating coupler connected to a 4 µm wide stripe waveguide. A focused mode in the planar waveguide section is excited by a collimated laser beam at a wavelength of $\lambda = 785.1$ nm and coupled into the waveguide stripe of 1.8 mm length. After exiting from the stripe waveguide, the divergent mode propagates through a second planar waveguide section to the output grating.

The attenuation of the waveguides was obtained by fitting an exponential decay curve to the intensity plot of the scattered light. First, a mode was excited in the slab waveguide with a wavelength $\lambda = 785.1$ nm employing a linear grating coupler. The attenuation of the mode without lateral confinement was 5.4 dB/cm. Obviously, this value is a lower limit for the

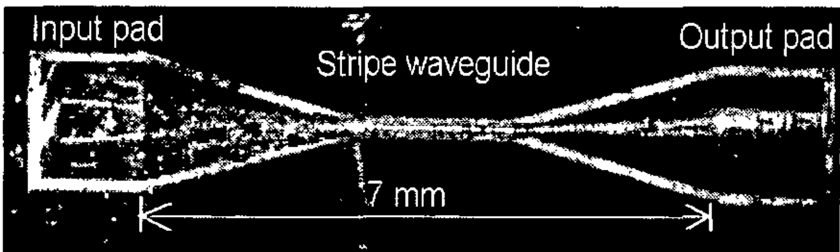

Fig. 33. 4 µm wide stripe waveguide with input and output grating pad

attenuation of the stripe waveguides, where additional scattering at the sidewalls occurs. The attenuation of thc 4 μm widc waveguide stripe was 8.5 dB/cm.

In Fig. 34, a scanning electron micrograph of an embossed Y-coupler in a polycarbonate substrate is shown. During the separation process, a "burr" has been formed in the upper arm of the interferometer, and the waveguides are slightly deformed. This demonstrates the necessity of a careful separation of the two structures as well as the requirement for smooth sidewalls, allowing a "gliding" separation of the master and the embossed structure . The edges of the structure are quite smooth, the roughness of the surface is below the resolution limit of the microscope.

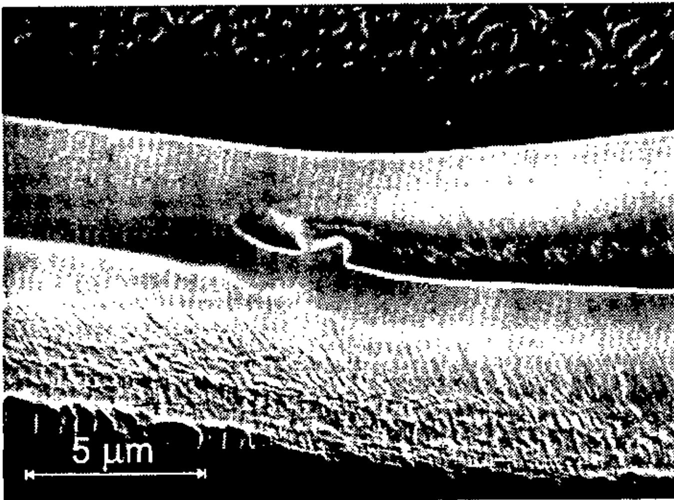

Fig. 34. SEM micrograph of a Y-coupler embossed into a polycarbonate substrate.

The Mach-Zehnder interferometer structures also were investigated by exciting modes via the focusing grating coupler. Fig. 35 shows a Mach-Zehnder interferometer consisting of 3 μm wide stripe waveguides. The

splitting of the light paths into the two arms at the first Y-coupler and their recombination in the second one is clearly visible. Additionally, the light guided in the subsequent part of the stripe waveguide can be observed, demonstrating the light transmission through the complete interferometer structure.

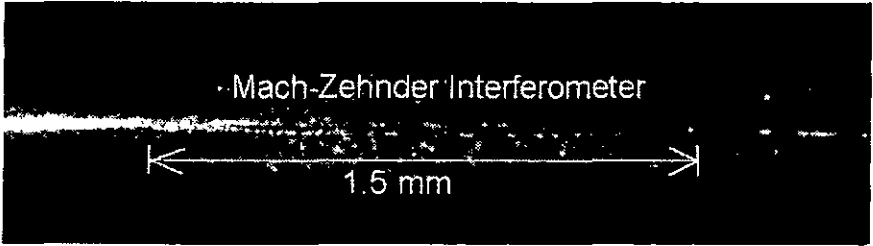

Fig. 35. Mach-Zehnder Interferometer structure guiding a TM0 mode at $\lambda = 785.1$ nm.

5.2. Refractometric measurements

5.2.1. Sensor response on different Ethanol/Water mixtures

5.2.1.1. Demonstration of sensor concept feasibility and measurement range

5.2.1.1.1. Waveguide parameters

First experiments to test the feasibility of the sensor based on the light pointer concept were performed with a chip consisting of a Ta_2O_5 film ($n_f = 2.2184$) deposited on a fused silica substrate ($n_s = 1.4571$) of 0.85 mm thickness by a shadow mask technique. In spite of the relatively deep gratings ($h_g \cong 12$ nm), the thickness taper characterization was performed based on the expressions given in Sec. 2 in the thin grating approximation. In order to minimize the systematic error introduced into the refractometer measurements by this approximation, the films were characterized with ethanol ($n_C = 1.3565$ @ 27.5°C), one of the test liquids, as cover medium. The refractive index n_C was determined by an Abbe refractometer with an accuracy of $3*10^{-4}$ and by applying the temperature correction coefficients found in [57, p. E-384]. Thc exponential model function

$$h_f = HF0 + HF1 \exp(y\,[\mu m] / HF2)\ [\mu m] \qquad (36)$$

was fitted to the experimental data to yield the solid curve shown in Fig. 36. The resulting values of the fit parameters were HF0 = 0.1289 μm, HF1 = -0.02128 μm, and HF2 = 4315 μm. An input coupling pad GP_i with a periodicity $\Lambda_i = 482.0$ nm and an output coupling pad GP_o with $\Lambda_o = 521.8$ nm were separated by a smooth waveguide section of 1 mm length. The input grating was illuminated at a fixed angle $\theta_i = 18.05°$ over a length $L_i \cong 0.5$ mm by a weakly focused beam at the wavelength $\lambda = 632.8$ nm through the substrate according to Fig. 12. Due to the large coupling coefficient of the doubly stacked gratings (cf. [3'', Fig. 2b]), the effective grating length L_g is expected to be substantially smaller than L_i.

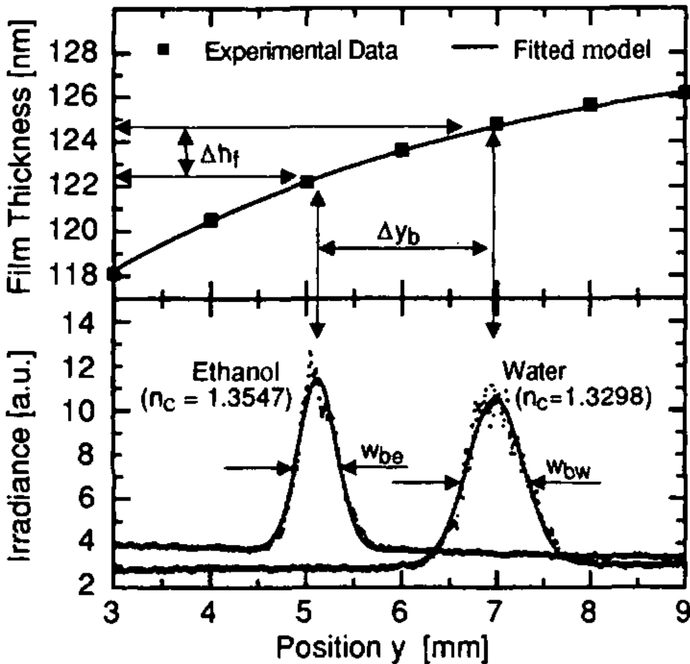

Fig. 36. Thickness taper profile (top) and Integrated optical light pointer irradiance (bottom) for a miniature refractometer chip based on a gradient in the effective waveguide index.

5.2.1.1.2. Refractometric experiments

The peaks shown in the lower part of Fig. 36, measured with the linear CCD array, correspond to the positions y_b of the IO light pointer for ethanol or water as the cover medium. Since an other setup at an other temperature was used to determine the thickness taper profile $h_f(y)$, the position of the "ethanol peak" was used to calibrate the position y = 5.12 mm on the y-axis corresponding to the refractive index $n_c = 1.3547$ for ethanol at the temperature of 32°C at which the experiments were performed. Due to a magnification factor of 1.62, the range of 6 mm shown in Fig. 36 amounts to a range of 9.72 mm on the CCD array, corresponding to 694 pixels. The solid lines shown in the lower part of the figure have been obtained by fitting the model function

$$I(y) = A + By + C\exp\left[-D(y - y_b)^2\right] \tag{37}$$

to the experimental data points. The function I(y) represents the irradiance distribution of the IO light pointer at the output coupler location.

Upon changing from ethanol to water, a shift of the IO light pointer position by an amount $\Delta y_b = 1.87$ *mm*, *corresponding to a thickness change* $\Delta h_f = 2.28$ nm was observed (cf. Fig. 36). What becomes obvious from the results is the effect of the exponential taper profile not only on the sensitivity, but also on the width of the peaks.

The smaller slope of the taper profile at the water peak position produces a higher sensitivity and an increase of the peak width. The experimentally determined full widths at half maximum of the peaks were $w_{be} = 467$ µm and $w_{bw} = 703$ µm for the ethanol and water peaks, respectively.

The position shift of the light pointer was in good agreement with the theoretically predicted values. Further measurements (see next section) were performed to determine the absolute accuracy of the refractive index values obtained from the light pointer positions.

5.2.1.2. Demonstration of sensor accuracy

5.2.1.2.1. Waveguide parameters

In this experiment, a waveguide consisting of a TiO_2 film deposited on a fused silica substrate was employed. As in the previous experiment, the values for the thickness h_f and the refractive index n_f of the waveguiding film were determined with ethanol, one of the test solutions, as cover medium to reduce the error introduced by modelling the waveguide in assumption of the thin grating limit.

The results of the sensor chip characterization for the TiO_2 waveguiding film are shown in Fig. 37.

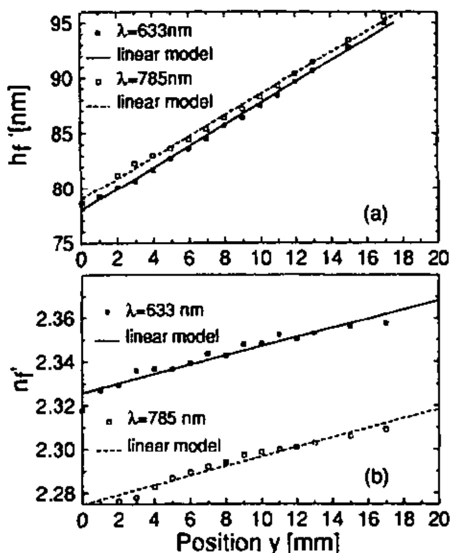

Fig. 37. Equivalent thicknesses (a) and refractive indices (b) of the waveguiding film used as sensor chip characteristics.

The measurements yielded a linear taper of the equivalent thickness

$$h_f'(y) = a + b * y \tag{38}$$

with coefficients a = 78 nm, b = $1.0*10^{-6}$ for λ = 632.8 nm and a = 79 nm, b = $1.0*10^{-6}$ for λ = 785.1 nm. The two equivalent thicknesses differ by less than 1 nm (cf. Fig. 37).

The corresponding results for the refractive index gradient

$$n_f'(y) = c + d * y \tag{39}$$

with coefficients, c = 2.33 and d = $2.1*10^{-3}$ mm^{-1} for λ = 632.8 nm, and c = 2.27 and d = $2.1*10^{-3}$ mm^{-1} for λ = 785.1 nm (see Fig. 37). The input and output waveguide gratings had periodicities of Λ_i = 481 nm for the input grating and Λ_o = 650 nm for the output grating coupler.

5.2.1.2.2. Refractometric measurements

For this measurement series, TM_0 light pointer modes were excited by illuminating the grating G_i by a HeNe laser beam ($\lambda = 633$ nm) at an angle of incidence $\theta_i = 12.2°$. Different mixtures of ethanol ('pro analysi' quality, purity > 99.8 %) with a small amount of water were pumped through the cell and the irradiance distribution on the line CCD was measured. For comparison, the refractive index of the mixture was determined by a commercial Abbe refractometer in a subsequent step. Fig. 38 shows the light pointer irradiance distributions, obtained by fitting the experimental data with a Gaussian model function. With 1 mm of grating length illuminated, the theoretical model given in [58] predicts a minimum beam width of ~ 200 μm, which is in good agreement with the observed widths > 250 μm. A change of the refractive index by 10^{-4} produces a light pointer shift of > 10 μm which is at the resolution limit of the present setup.

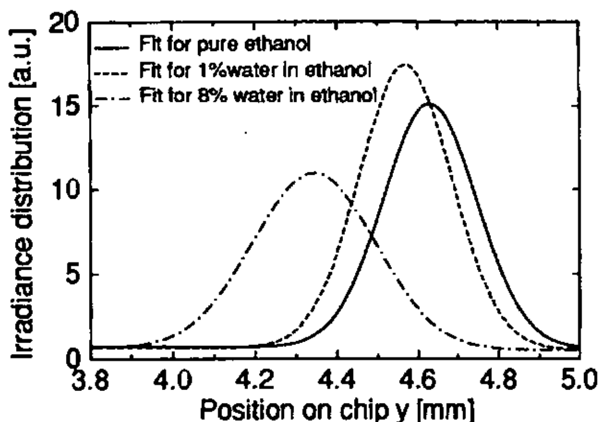

Fig. 38. Variation of the light pointer position for different cover media.

The refractive index of an ethanol-water mixture rises upon adding small amounts of water to the ethanol, until the azeotropic concentration is reached, then it decreases to the index of pure water. Fig. 39 shows the rise of the refractive index upon adding water to ethanol [60]. The values at 633 nm plotted in Fig. 39 were determined based on the light pointer positions y_b (n_c), measured for the TM_0 mode. For this purpose, the linear regression curves shown in Fig. 39, representing the refractometer chip parameters, were used. For the mixtures considered here, the optical dispersion does not differ much from that of pure ethanol. Therefore, the original n_D (λ = 589.3 nm) values from the Abbe refractometer measurements were dispersion corrected to the wavelength of the HeNe laser using a fit to the literature data [59] for pure ethanol. The resulting values are included in Fig. 39. Repeating the measurements, an accuracy of about $2*10^{-4}$ was observed for both the Abbe refractometer and the IO chip. First experiments at the wavelength λ = 785 nm, also performed for the TM_0 mode, show a similar change of the evaluated cover refractive index. The angle of incidence was changed to θ_i = - 8.8° in order to keep the pointer position in the same chip region. If the whole width of the present refractometer chip (17 mm) is used for the measurements, a full range of the absolute refractive index of about 0.19 can be achieved per fixed angle of incidence.

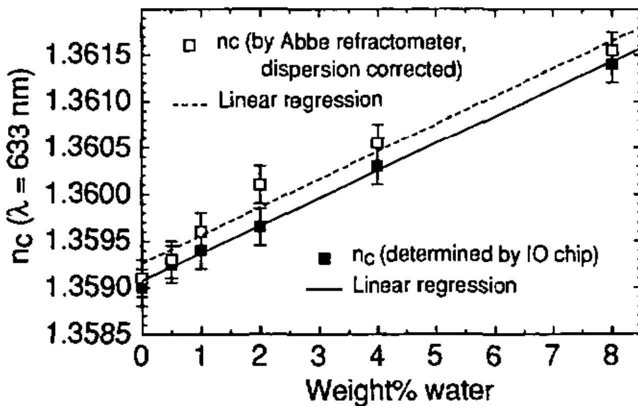

Fig. 39. Comparison of absolute refractive indices determined by the IO chip (■) and by a commercial Abbe refractometer (□).

5.2.1.3. Dynamic sensor measurements

Dynamic measurements, where the position of the IO light pointer was continuously monitored during a repcated switching between ethanol and water, have been performed employing the sensor chip characterized in 5.2.1.1 and using the setup shown in Fig. 12, but with the CCD array replaced by a position sensitive detector (PSD, Hamamatsu S3932). The top part of Fig. 40 shows the control signals used for switching betwecn an ethanol or water flow through the refractometer cell. The resulting output signal, created by the IO light pointer beam moving over the PSD surface, is shown in the lower part of the figure. It was obtained by feeding the output of the PSD circuit into a digital oscilloscope with an 8 bit resolution.

Two diffcrent times characterizing the sensor response are defined in Fig. 40. The time delay τ_d between thc edge of the valve control signal and the beginning of the sensor reaction originates essentially from the valve switching time and the time the liquid needs to flow from the valve to the sensor cell. A value $\tau_d \cong 200$ ms was observed at a flow speed of 2m/s in the connecting tube and 0.3m/s in the test cell. The rise time τ_r, describing the time for a signal change between 10% and 90%, was ~350 ms.

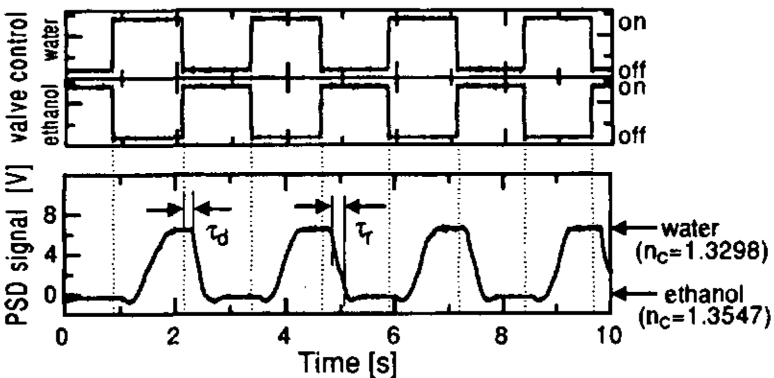

Fig. 40. Output signal (bottom) and valve control signals (top) for an IO light pointer transducer chip.

It is mainly determined by the time required to completely exchange the two pure liquids in the cell.

An output signal undershoot of ~8% with a duration of ~200 ms is reproducibly observed upon reaching and leaving the pure ethanol condition. This corresponds to an apparent transient increase by $\Delta n_C \approx 2.4*10^{-3}$. According to the results shown in chapter 5.2.1.2.2, a difference of this magnitude would correspond to a water content of about 8 %. Therefore, this transient refractive index excursion corresponds well to the mixtures dynamically sweeping through the azeotropic concentration. However, a lower signal excursion results from the bandwidth of the PSD electronics being too low to follow the very fast light pointer displacement.

5.2.2. Measurements of chemical quantities

For performing chemical measurements, the chemically sensitive membrane described in Chapter 3.1.3 was deposited on a waveguide consisting of a tapered TiO_2 film deposited on a quartz substrate with etched gratings. Two different gratings having the periods $\Lambda_1 = 650.4$ nm and $\Lambda_2 = 480.0$ nm had been etched into the substrate. Due to problems encountered with direct coating of the membranes on the TiO_2 film (cf. Chapter 4.7), the chip had been coated with a 20 nm thick SiO_2 intermediate layer. The spin coating was performed at 800 rotations per minute for 45 seconds immediately after filtering the membrane cocktail.

After installing the chip in the measurement cell, the membrane had to be 'conditioned', i.e. a buffer solution was pumped into the cell to protonate the ionophore, while at the same time positively charged metal ions were removed from the membrane into the solution.

In first experiments performed at a wavelength of $\lambda = 690$ nm, modes were excited by illuminating one of the grating couplers as depicted in Fig. 12. However, it was not possible to observe light coupled out from the mode via the second grating. This might be due to the grating distance of 1 mm in combination with the high absorbance of the membrane at this wavelength. For this reason, the operating wavelength was changed to $\lambda = 785$ nm, where the absorption measurement displayed in Fig. 5 showed lower values. Additionally, the scattering due to waveguide imperfections is lower at this wavelength.

The incident TE-polarized laser beam illuminated the grating of period $\Lambda_1 = 650.4$ nm at an angle $\Theta_i = 45.1°$. By this, the TE_0 mode was locally excited by the first diffraction order of the grating, producing an integrated optical light pointer (cf. Chapter 3.2.3). Since the mode coupled out from the output grating was only faintly visible due to waveguide losses even at this wavelength, the second diffraction order of the input grating was observed for the measurements. The linear CCD detector was placed into the output beam of the second diffraction order at an angle of 29.9°.

The irradiance on the linear CCD device was scanned continuously by a computer controlled setup, as described in Chapter 3.2.5.2. The position of the maximum of a Gaussian curve fitted to the irradiance was written to a file approximately every three seconds. Five subsequent measurements were averaged to obtain a data point in the position signal displayed.

In these first measurements, solutions with different concentrations of Ca-ions were pumped through the measurement cell. For a first demonstration of the sensor principle, Ca^{2+}-concentrations of 10^{-5} mol/l and 10^{-1} mol/l were chosen. An amount of 15 ml test solution was pumped through the cell of about 15 µl volume during each liquid exchange phase, so that a complete exchange of the cell content could be assumed. The pumping then was stopped and the solution remained in the cell for 10 minutes, which was expected to be a sufficient period of time for the membrane to get close to the equilibrium state. After this waiting period, new test solution was inserted. The time for insertion of the new test liquid was about 30 seconds.

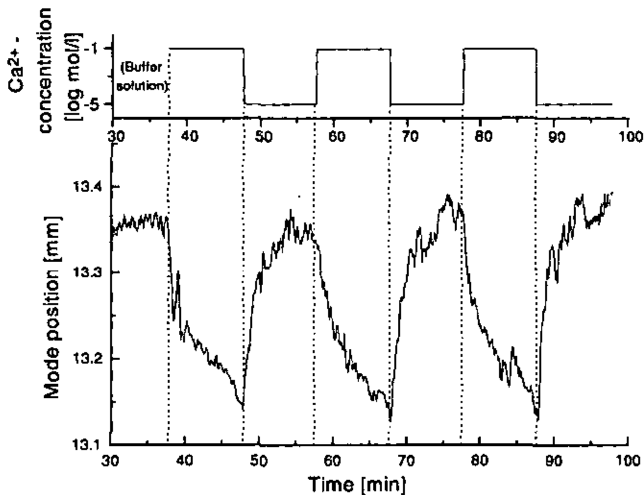

Fig. 41. Concentration of Ca-ions in test solution (top) and evaluated light pointer position (bottom).

The results of the position measurements of the light coupled out from the integrated optical light pointer are shown in Fig. 41. In the first phase, the membrane was in an equilibrium state being in contact with buffer solution without any Calcium content for about 30 minutes. Subsequently, the test solution was switched several times between the 10^{-1}-molar Ca -solution and the 10^{-5}-molar Ca -solution to test the repeatability of the experiment and the long-term stability of the setup.

The position signal depicted in Fig. 41 shows that the chosen cycle period of ten minutes is too short for the membrane to reach the equilibrium state for both concentrations. The system shows a slightly longer time constant for switching from the high to the low concentration than vice versa. It can also be seen that the light pointer positions are quite reproducible when the measurement is repeated several times. The measurement range tested can easily be subdivided into at least ten or twenty steps, leading to a resolution of about one fifth of a decade of concentration for the present setup.

The measured shift in the light pointer position of $\approx 200\ \mu m$ upon varying the Ca-concentration by four decades corresponds to a change in refractive index of the chemically sensitive membrane of about $4*10^{-3}$. It is evident from the measurement that a larger excursion of the lateral pointer position will occur if more time is allowed for the system to reach the equilibrium state. This change is in the same order of magnitude as the results presented by Freiner et al. in [13], where a change in the membrane's refractive index of $1.3*10^{-3}$ per decade of Ca-concentration was reported for a wavelength of 688 nm.

The measurement shows both the suitability of this sensor arrangement for sensitive chemical measurements as well as its possible application for measuring dynamic effects of the sensor membrane.

It was also tested to deposit the chemically sensitive membrane on TiO_2 - coated polycarbonate substrates. For stability purposes, these chips of 0.25 mm thickness are usually glued on small glass slides using UV-curable epoxy resin in our laboratory. Unfortunately, the solvent of the membranes (Tetrahydrofuranc) attacks the epoxy, leading to opaque areas under the chip. For future measurements with sensor membranes coated on these chips, the epoxy has to be protected laterally against the solvent.

6. Conclusions and Outlook

In this thesis, different schemes for miniature integrated optical sensors suited for miniaturizing the complete sensor system were proposed and investigated. The sensors were based on measuring the influence of external parameter changes on the evanescent field of a guided wave.
The first system was based on the spatial variation of the resonance condition for coupling into a planar or slightly tapered waveguide via a grating coupler, thus exciting a so-called 'integrated optical light pointer'. The refractometric experiments performed on a setup of this type showed that the system is suitable for building compact refractometers with fast response time and high precision [60], the accuracy being comparable to commercial systems. For a higher precision or a larger range of refractive indices to be measured, the waveguide simulation used for the re-calculation of the cover refractive index from the waveguide parameters and the light pointer position has to be extended to model gratings with finite depth [18].

The use of sensitive membranes as cover of the waveguide to convert concentration changes of a specific chemical substance into a refractive index change of the cover medium was also investigated. After solving problems with the coating process and chemical interactions between waveguide and sensor membrane, a measurement of Ca-ion concentration in a solution was performed based on a waveguide with thickness variation. The sensor response on the change between a solution with 10^{-1} and a 10^{-5} mol Calcium per litre as test solutions was quite high, so that a resolution of the system of about 0.2 decades of Ca-ion concentration can be expected. In subsequent works, membranes of the same type being sensitive to heavy metals might be applied to the measurement chips.

Another approach for the realization of highly sensitive integrated optical sensors are interferometric structures. A new method was developed to produce Mach-Zehnder interferometer structures together with focusing grating couplers for input and output in a single hot embossing step into a polycarbonate foil followed by waveguide coating. Samples of this type were fabricated and characterized; the input and output of a collimated free-

space beam to a 4 µm wide stripe waveguide was experimentally demonstrated as well as the light transmission through a Mach-Zehnder interferometer formed of 3 µm wide stripe waveguides. This approach is very promising for the fabrication of very sensitive low-cost sensors, since not only the chip itself is a low-cost device, but the integration of the focusing coupling function into the chip allows to reduce the demands for external optical elements and adjustment devices.

7. References

1 R.E. Kunz, "Totally Integrated Optical Measuring Sensors," Proc. SPIE, Vol. 1587, 98-113, (1991).

2 M.T. Gale, L.G. Baraldi and R.E. Kunz, "Replicated Microstructures for Integrated Optics," Proc. SPIE, Vol. 2213, 2-10, (1994).

3 R.E. Kunz, J. Edlinger, B.J. Curtis, M.T. Gale, L.U. Kempen, H. Rudigier, and H. Schütz, "Grating Couplers in Tapered Waveguides for Integrated Optical Sensing," Proc. SPIE, Vol. 2068, 313-325 (1994).

4 M.V. Klein and T.E. Furtak, *Optik*, (Springer-Verlag Berlin Heidelberg, 1988), pp. 255.

5 P.K. Tien, "Integrated Optics and New Wave Phenomena in Optical Waveguides," Reviews of modern physics, Vol. 49, No. 2, 361-383, (1977).

6 H. Nishihara, M. Haruna and T. Suhara, *Optical Integrated Circuits*, (McGraw-Hill, New York, 7-14, 1989).

7 P.K. Tien, R. Ulrich and R.J. Martin, "Modes of Propagating Light Waves in Thin Deposited Semiconductor Films," Applied Physics Letters, Vol. 14, 291, (1969).

8 W. Lukosz and K. Tiefenthaler, "Directional Switching in Planar Optical Waveguides Effected by Adsoption-Desorption Processes," Second European Conference on Integrated Optics 1983, Florence, IEE Conf. Publ. No.227, IEE, London, 152-155, (1983).

9 K. Tiefenthaler and W. Lukosz, "Integrated Optical Switches and Gas Sensors," Optics Letters, Vol. 9, 137-139, (1984).

10 K. Tiefenthaler and W. Lukosz, "Sensitivity of grating couplers as integrated-optical chemical sensors," Journal of the Optical Society of America B, Vol. 6, No. 2, (1989).

11 R.E. Kunz, C.L. Du, J. Edlinger, H.K. Pulker and M. Seifert, "Integrated Optical Sensors Based on Reactive Low-voltage Ion-plated Films," Sensors and Actuators A, Vol. 25-27, 155-159, (1991).

12 W.E. Morf, K. Seiler, B. Rusterholz and W. Simon, "Design of a Calcium-Selective Membrane Based on Neutral Ionophores," Analytical Chemistry, Vol. 62, No. 7, 738-741, (1990).

13 D. Freiner, R.E. Kunz, D. Citterio, U.E. Spichiger and M.T. Gale, "Integrated Optical Sensors Based on Refractometry of Ion-Selective Membranes," Sensors and Actuators B, Vol 29, 277-285, (1995).

14 M.L. Dakss, L. Kuhn, P.F. Heidrich and B.A. Scott, "Grating Coupler for Efficient Excitation of Optical Guided Waves in Thin Films," Applied Physics Letters, Vol. 16, No. 12, 523-525, (1970).

15 K. Knop, "Rigorous diffraction theory for transmission phase gratings with deep rectangular grooves," J. Opt. Soc. Am., Vol. 68, No. 9, 1206-1210, (1978).

16 R.H. Morf, "Exponentially convergent and numerically efficient solution of Maxwell's equations for lamellar gratings," J. Opt. Soc. Am. A, Vol. 12, No. 5, 1043-1056, (1995).

17 M. Born and E. Wolf, *Principles of Optics*, (Sixth (corrected) Edition, Pergamon Press, 312-315, 1989).

18 R.E. Kunz, J. Dübendorfer and R.H. Morf, "Finite grating depth effects for integrated optical sensors with high sensitivity," Biosensors and Bioelectronics, Vol. 11, No. 6/7, 653-667, (1996).

19 K. Tiefenthaler and W. Lukosz, "Grating Couplers as integrated optical humidity and gas sensors," Proc. of the sixth conference on thin films, Stockholm, Sweden, 205-211, (1985).

20 W. Lukosz, Ph.M. Nellen, Ch. Stamm and Weiss, "Output grating couplers on planar waveguides as integrated optical chemical sensors," Sensors and Actuators B, No. 1, 585-588, (1990).

21 W.H. Press, B.P. Flannery, S.H Teukolsky and W.T Vetterling, *Numerical Recipes,* (Cambridge University Press, 1986), 498-546.

22 Hamamatsu Technical Data Sheet for One-Dimensional Position Sensitive Detectors, Hamamatsu Photonics KK, Hamamatsu City, Japan, (1990).

23 Melles-Griot Optics Guide 5, ISSN 1051-4384 1876 115M 1290, p.17.5-17.11, © Melles-Griot 1990.

24 B.H. van der Schoot, S. Jeanneret, A. van den Berg and N.F. de Rooij, "Microsystems for Flow Injection Analysis," Analytical Methods and Instrumentation, Vol. 1, No. 1, 38-42, (1993).

25 L. Zehnder, Zeitschrift für Instrumentenkunde, Vol. 11, 275, (1891).

26 L. Mach, Zeitschrift für Instrumentenkunde, Vol. 12, 98, (1892).

27 A. Brandenburg, R. Edelhäuser and F. Hutter, "Gas sensor based on an integrated optical interferometer," Proc. SPIE, Vol. 1510, 138-143, (1991).

28 L. Baraldi, R.E. Kunz and J. Meissner, "High-precision molding of integrated optical structures," Proc. SPIE, Vol. 1992, 21-29, (1993).

29 R.E. Kunz, J. Edlinger, Sixt and M.T. Gale, "Replicated Chirped Waveguide Gratings for Optical Sensing Applications," Sensors and Actuators A, Vol. 47, 482-486 (1995).

30 R.E. Kunz and J.S. Gu, "Design of Integrated Optical Couplers and Interferometers Suitable for Low-cost Mass Production," Proc. ECIO'93, 14-36/37, (1993).

31 R. Pregla and W. Pascher, "The Method of Lines," in *Numerical Techniques for Microwave and Millimeter Wave Passive structures, (T. Itoh (Hrsg.), Wiley, 1989).*

32 S. Ura, T. Suhara, and H. Nishihara, "An Integrated-Optic Disk Pickup Device," Journal of Lightwave Technology, Vol. LT-4, NO. 7, 913-918, (1986).

33 L.G. Baraldi, *Heissprägen in Polymeren für die Herstellung integriert-optischer Systemkomponenten,* PhD Thesis ETH Nr. 10762, Swiss Federal Institute of Technology (ETH), Zurich.

34 H. Hosokawa, N. Horie and T. Yamashita, "Simultaneous fabrication of grating couplers and an optical waveguide by photopolymerization," Integrated Photonics Research, IEEE-LEOS and OSA Photonics Reports, Technical Digest Series, ,Vol. 5, 26-27, (1990).

35 H. Hosokawa, N. Horie and T. Yamashita, "Mass-producible Optical Guided-wave Devices Fabricated by Photopolymerization," Proc. SPIE, Vol. 1559, 229-237, (1991).

36 J.-P. Weber, "Device Design Using Gaussian Beams and Ray Matrices in Planar Optics," IEEE Journal of Quantum Electronics, Vol. 30, No. 10, 2407-2416, (1994).

37 T. Tamir, *Integrated Optics*, (Topics in applied physics, Vol. 7, 2nd edition, Springer Verlag, Berlin, 1985), 98-118.

38 R. Waldhäusl, E.-B. Kley P. Dannberg, A. Bräuer and W. Karthe, "Grating Couplers in Planar Polymer Waveguides with Beam Shaping Properties," Proc. SPIE, Vol. 2213, 122-132, (1994).

39 L.M. Johnson, F.J. Leonberger and G.W. Pratt, Jr., "Integrated optical temperature sensor," Applied Physics Letters, Vol. 41, No. 2, 134, (1982).

40 W. Menz and P. Bley, *Mikrosystemtechnik für Ingenieure*, VCH Verlagsgesellschaft, Weinheim, 1993.

41 R.D. Te Kolste, W.H. Welch and M.R. Feldman, "Injection molding for diffractive optics," Proc. SPIE, Vol. 2404, 129-131, (1995).

42 M.T. Gale, "Replication", in *Micro-optics : Elements, systems and applications*, H.P. Herzig (Ed.), Taylor and Francis, 1996.

43 M. Miller and S. Skalsky, "Chirped and Curved Grating Coupler Focusing Both Outgoing Beam and Incoming Wave," Optics Communications, Vol. 33, No. 1, 13-16, (1980).

44 D. Heitmann and R.V. Pole, "Two-Dimensional Focusing Holographic Grating Coupler," Applied Physics Letters, Vol. 37, No. 7, 585-587, (1980).

45 D. Heitmann and C. Ortiz, "Calculation and Experimental Verification of Two-Dimensional Focusing Grating Couplers," IEEE Journal of Quantum Electronics, Vol. QE-17, No. 7, 1257-1263, (1981).

46 T. Suhara, H. Nishihara and J. Koyama, "High-Performance Focusing Grating Coupler Fabricated by Electron-Beam Writing," presented at Topical Meet. Integrated Guided-Wave Optics, Kissimmee, FL, paper ThD4, April 24-27, (1984).

47 J.L. Vossen and W. Kern, *Thin Film Processes*, (Academic Press, New York, 529, 1978).

48 T. Hwang, G.W. Wang, Y. Chang, and C.L. Lau, "Comparison of Single and Tri-Layer Technologies for Volume Production of Sub-Half Micron Gate GaAs MESFETs," Journal of the Electrochemical Society, Vol. 139, No. 2, 625-628, (1992).

49 H.E.G. Arnot, H.P. Zappe, J.E. Epler, B. Graf, R. Widmer and H.W. Lehmann "Extremely Smooth Sidewalls for GaAs/AlGaAs Ridge Waveguides," Electronic Letters, Vol. 29, No. 12, 1131-1133, (1993).

50 H.W. Lehmann, "Plasma-Assisted Etching," in *Thin Film Processes II*, (Academic Press, New York, 673-748, 1991).

51 L.M. Eprath and E.J. Petrilio, "Parameter and Reactor Dependence of Selective Oxide RIE in CF_4 and H_2," Journal of the Electrochemical Society, Vol. 129, No. 10, 2282-2287, (1982).

52 R. Brugger, *Die galvanische Vernickelung*, 2nd edition , (Eugen G. Leuze Verlag, Saalgau, Germany, 1984), 23-26.

53 S. Musikant, *Optical Materials - An introduction to selection and application*, (Marcel Dekker, Inc., New York, 1985), 149-151.

54 R. Jaszewski, "Study of physico-chemical properties of thin anti-adhesive teflon films on embossing nickel shims used in the replication

of microstructures for optics," Diploma thesis at the Federal Institute of Technology Lausanne (EPFL), Switzerland, 21-23, (1996).

55 H.K. Pulker, *Coatings on Glass*, (Elsevier Science Publishers BV, Amsterdam, The Netherlands, 1984).

56 J. Edlinger, Balzers AG, Liechtenstein, private communication.

57 *CRC Handbook of Chemistry and Physics*, 70th edition, (CRC Press Inc., Boca Raton, 1989).

58 R.E. Kunz and L.U. Kempen, "Miniature Integrated Optical Sensors," Proc. SPIE, Vol. 2068, 69-86, (1994).

59 R.C. Wilhoit and B.J. Zwolinski, "Physical and Thermodynamic Properties of Aliphatic Alcohols," Journal of Physical and Chemical Reference Data, Vol 2, Suppl. No. 1, (1973).

60 L.U. Kempen and R.E. Kunz, "Miniature Integrated Optical Refractometer Chip," Proc. SPIE, Vol. 2208, 124-129, (1994).

Title figures : Embossed polycarbonate substrate with various waveguide and interferometer structures combined with focusing grating couplers, excited by a HeNe-laser beam (Fig. 32) and scheme of a Mach-Zehnder interferometer sensor with focusing input and output couplers (Fig. 22).